Spatial Chirp-Based Optimization for Analog Beamforming in Line-of-Sight Terahertz Ultra-Wideband Phased Tx Array Systems

Xingyu Chen, *Student Member, IEEE*, Li Zhang, *Senior Member, IEEE*, Pingzhi Fan, *Fellow, IEEE*

***Abstract*—THz ultra-wideband wireless communication is emerging as a critical technology for future 6G networks, due to its vast untapped frequency spectrum. The use of phased antenna arrays is highly effective in mitigating the significant attenuation of THz signals, thereby ensuring high-quality communication. Analog phased arrays with well-designed phase shifters concentrate signal gain spatially to compensate for propagation loss. However, conventional narrowband analog beamforming compromise ultra-wideband performance. In this paper, we address the degradation problem of analog beamforming in line-of-sight THz ultra-wideband systems that optimizes throughput across various application scenarios. We apply the stationary phase method to derive initial phase function solutions. We then develop an iterative algorithm to maximize throughput and design optimal phase shifters. The effectiveness and advantages of our proposed methods are demonstrated through simulation results, which show significant improvements in throughput and reductions in bit error rate compared to state-of-the-art wideband analog beamforming methods.**

***Index Terms*—analog beamforming, terahertz, ultra-wideband, optimization, spatial chirp.**

I. Introduction

In recent years, the growing demand for greater capacity, faster transmission speeds, and better overall network performance has been driving the exploration and adoption of higher wireless frequency bands [1], [2]. Spectrum scarcity necessitates utilizing 30-300 GHz millimeter-wave (mmWave) and 0.1-10 THz bands [3]. Higher frequencies enable ultra-high-speed transmission essential for emerging technologies [4], e.g., augmented reality (AR), virtual reality (VR), and autonomous vehicles (AVs). Shorter wavelengths enable smaller antennas and more precise beamforming, improving spatial resolution [5], which is particularly advantageous for applications in radar, medical imaging, and satellite communications [6]. Advancements in metasurface and chip technologies have made mmWave and THz systems increasingly practical [7], [8].

However, extreme propagation attenuation presents significant challenges for mmWave and THz systems [9], [10]. Large-scale antenna arrays mitigate attenuation through beamforming, making them key for 5G-beyond networks [11], [12]. By adjusting per-element phase, these arrays spatially focus signal gain into directed beams. Analog beamforming provides array gain and directional energy focusing to mitigate interference [13]. However, in wideband system, phased arrays must use one group of phase shifters across all sub-bands due to hardware constraints [14]. This challenges wideband communications, as conventional phase shifters use fixed patterns optimized for center frequency [15]. At other frequencies, beam squint deteriorates performance, worsening with frequency deviation [16]. This phenomenon is manifested as beam squint in the mmWave band [17], and the relatively narrow bandwidth enables beam squint mitigation via hybrid beamforming (HBF) [18], [19]. However, in THz ultra-wideband (UWB)systems, the issue escalates to beam splitting [20], causing substantial performance degradation [21].

A. Related Works

Numerous methods have been proposed to mitigate this problem from both hardware and algorithm perspectives, showing notable effectiveness in the mmWave frequency range. On the hardware side, digital beamforming and true-time-delay (TTD)-based beamforming techniques have attracted significant attention due to their impressive performance. Fully digital beamforming aggregates all subcarriers via IFFT and enables per-subcarrier design, eliminating beam splitting [22]. However, requiring one RF chain per antenna makes this impractical for massive arrays due to cost and power consumption [23]. HBF reduces RF chain count to balance performance and cost. However, ADC/DAC power scales exponentially with resolution and linearly with sampling rate. THz UWB requires tens to hundreds of Giga-samples per second, making even hybrid architectures power-prohibitive (hundreds of watts) for mobile devices [24], [25], [26]. Frequency-selective TTD architectures adjust per-antenna RF delay for different subcarriers but incur higher cost, size, and power [27], [28]. TTD-analog hybrids balance power and beam splitting mitigation but remain challenging for THz ultra-massive arrays [29], [30], [24]. Thus, analog beamforming's single RF chain drastically reduces power and cost while providing essential array gain, making it considerable for THz UWB systems.

Algorithm-based approaches include beam broadening, which divides arrays into sub-arrays to widen beams without structural modifications [31]. However, sparser beams reduce energy efficiency [19]. Adaptive beamforming is proposed to dynamically adjusts weights across subcarriers for better alignment [17]. A sparse array method with adjustable antenna spacing is also proposed to improve alignment [32]. Similarly, [28] proposed a semi-definite relaxation-based method, but

the high complexity makes it challenging to handle massive arrays. Additionally, Machine learning (ML) has been investigated in this field. However, it must learn channels across massive bandwidths, exponentially increasing data and complexity requirements [32]. These approaches mainly target mmWave bands, but THz channels differ fundamentally. THz signals experience much higher attenuation, requiring near-field analysis [33], and depend heavily on LoS channels [34]. These differences make mmWave channel models unsuitable for THz UWB, limiting the effectiveness of these approaches [35]. For instance, ML models trained on mmWave channels would fail to address beam splitting in THz UWB scenarios.

Spatial chirp determines phase shifters by spatially dependent phase function. It was initially introduced for far-field narrowband scenarios [36] and enhanced for 5G radio systems [37]. The stationary phase method (SPM) was applied to design spatial chirp for circular planar array in near-field THz UWB systems [38]. Lately, this method was extended to reconfigurable intelligent surface (RIS)-assisted systems [39]. However, no work uses spatial chirp to systematically optimize throughput for both uniform linear and planar array (ULA and UPA) configurations. Moreover, the SPM has key limitations: it is used to uniform power spectrum but not optimize throughput, it requires approximations that compromise accuracy, and no closed-form solution in near-field UPA scenarios.

B. Contributions

We leverage spatial chirp to systematically develop an optimization method for analog beamforming in LoS THz UWB communication systems, aiming to eliminate the beam splitting effect and maximize system throughput. The proposed method considers both phased ULA and UPA at the transmitter, and is applicable in both far-field and near-field scenarios. Distinguishing our work from existing studies, e.g., [38], which only consider a uniform power spectrum, we have a specific objective function, i.e., system throughput, for maximization. This ensures that the proposed method can lead to optimal system performance. A key innovation is that we represent phase functions as polynomials rather than merely relying on traditional closed-form solutions that can only be used for restricted scenarios. This enable us to further develop an iterative algorithm to optimize the polynomial coefficients for different scenarios with reduced complexity. The regular geometry of ULA and UPA arrays is particularly well-suited to this method, allowing the spatial chirp to be characterized by just a few polynomial coefficients. For other array geometries, e.g., circular, cylindrical, and conformal arrays, it is difficult to define the spatial domain and apply a polynomial series to construct spatial chirp. The primary advantage of this spatial chirp approach is its efficiency for large-scale antenna arrays in THz communications, as it transforms the optimizing of massive phase sequences to that of a few coefficients, thereby significantly reducing computational complexity. The main contributions are summarized as follows:

- The degradation problem of analog beamforming in LoS THz UWB systems is overcome by proposing a spatial chirp-based method to maximize the throughput across various application scenarios. The initial phase functions are achieved by applying the SPM to both ULA and UPA configurations for their phase functions. These solutions can achieve a more uniform received signal power spectrum in order to ensure a good wideband beamforming performance for the initialization.
- To guarantee optimal throughput, we formulate the design of phase function as a maximization problem of system throughput. To make the problem tractable, we represent phase functions using polynomial expansion and define the optimization variables as polynomial coefficients. An iterative algorithm is developed to solve the throughput maximization problem, initialized with the SPM-based initial phase functions. The optimization algorithm is applicable to both ULA and UPA configurations across far-field and near-field regimes.
- We evaluate the performance of the proposed method through comprehensive simulations, demonstrating its superiority over conventional solutions [15] and state-of-the-art wideband analog beamforming methods, including the singular value decomposition (SVD)-based method in [40] and the virtual sub-array (VSA)-based method in [31]. Key performance metrics, including throughput and bit error rate (BER), are evaluated in both far-field and near-field scenarios for both ULA and UPA configurations.

The remainder of the paper is organized as follows. Section II presents system models. Section III derives initial phase functions. Section IV formulates the optimization problem and iterative algorithm with recommended parameters. Section V presents simulations and Section VI concludes.

II. System Models

We consider downlink LoS THz UWB phased array systems with N_{T} Tx antennas and one Rx antenna using OFDM with bandwidth BW, center frequency f_{c}, and S_{c} evenly distributed subcarriers at frequencies $f_m = f_{\mathrm{c}} - \frac{BW}{2} + \frac{BW}{S_{\mathrm{c}}}(m - \frac{1}{2}), m = 1, 2, \ldots, S_{\mathrm{c}}$. All antennas are isotropic with unit gain and $\frac{\lambda}{2}$ spacing [41], where λ is the wavelength at f_{c}. The Tx-Rx distance is D. Far-field ($D > D_{\mathrm{R}}$) has planar wavefronts and near-field ($D \leq D_{\mathrm{R}}$) has spherical wavefronts, where $D_{\mathrm{R}} = \frac{2L^2}{\lambda}$ is the Rayleigh distance [42] and L is array aperture. We assume known Rx location and Tx layout via localization [43] and channel estimation [44]. The model is static with time-invariant distance D, angle of departure (AoD), and channel. We consider only the dominant LoS channel [34] with accessible channel state information (CSI) [45]. The wideband channel $\vec{H}(f)$ comprises geometry-based LoS channel transfer functions (CTFs) $h_n(f)$ for $n = 1, 2, \ldots, N_{\mathrm{T}}$ [46], determined by pathloss $PL_n(f)$ and phase delay $\tau_n(f)$ [46]

$$\vec{H}(f) = [h_n(f)]_{N_{\mathrm{T}} \times 1}\,, \tag{1}$$

$$h_n(f) = PL_n(f) e^{-j\tau_n(f)}, \tag{2}$$

$$PL_n(f) = \frac{c}{4\pi f \mu_n}, \tag{3}$$

$$\tau_n(f) = \frac{2\pi f \mu_n}{c}, \tag{4}$$

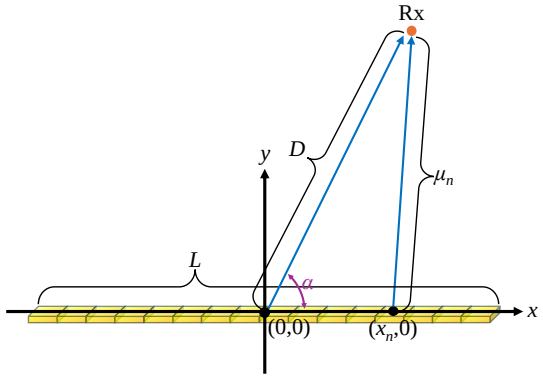

(a) Phased ULA Tx

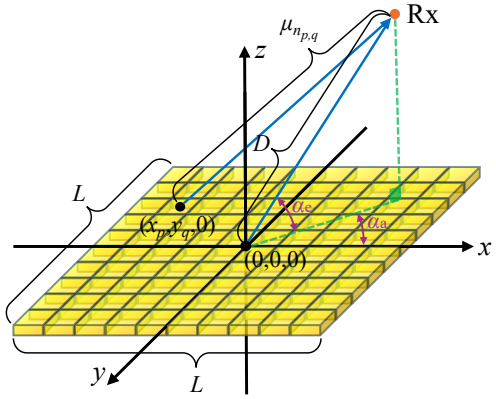

(b) Phased UPA Tx

Fig. 1. Phased ULA (a) and UPA (b) Tx system models.

where μ_n is signal propagation distance between the n-th Tx antenna and the Rx. The system model, phase shifters, equivalent channel gain, and propagation distance function will be described respectively for the ULA and UPA scenarios in the following subsections.

A. ULA System Model

The phased ULA Tx is illustrated in Fig. 1(a), with the array positioned along the x-axis and centered at the origin $O_{\mathrm{L}} = (0,0)$. The central coordinate of the n-th antenna is $C_n^{\mathrm{L}} = (x_n, 0)$, where x_n is the spatial variable of the ULA, $x_n = \frac{\lambda}{2}(n - \frac{1}{2}) - \frac{L}{2}$, and $L = \frac{\lambda}{2}N_{\mathrm{T}}$. The coordinate of Rx is given by $C_{\mathrm{Rx}}^{\mathrm{L}} = (D\cos(\alpha), D\sin(\alpha))$, where $\alpha \in [0, \pi]$ is the AoD.

The normalized ULA phase shifters, denoted as $\vec{\phi}_{\mathrm{L}}$, corresponding to $n = 1, 2, \ldots, N_{\mathrm{T}}$ Tx antennas, is given by

$$\vec{\phi}_{\mathrm{L}} = \frac{1}{\sqrt{N_{\mathrm{T}}}} \left[e^{j\varphi_{\mathrm{L}}(x_n)} \right]_{N_{\mathrm{T}} \times 1}, \tag{5}$$

where $\varphi_{\mathrm{L}}(x)$ is the ULA spatially dependent phase function that will be designed to attain maximal throughput.

The equivalent channel gain as a function of f, denoted as $g_{\mathrm{L}}(f)$, is given by

$$g_{\mathrm{L}}(f) = \vec{H}(f)^T \vec{\phi}_{\mathrm{L}}. \tag{6}$$

It can be written in summation by substituting the expressions of $\vec{H}(f)$ and $\vec{\phi}_{\mathrm{L}}$

$$g_{\mathrm{L}}(f) = \frac{1}{\sqrt{N_{\mathrm{T}}}} \sum_{n=1}^{N_{\mathrm{T}}} \frac{c}{4\pi f \mu_n} e^{j\varphi_{\mathrm{L}}(x_n)} e^{-j\frac{2\pi f \mu_n}{c}}. \tag{7}$$

In the far-field planar wavefront [47], μ_n is determined by taking x_n into the far-field ULA distance function, denoted as $\mu_{\mathrm{FL}}(x)$

$$\mu_{\mathrm{FL}}(x) = D - \cos(\alpha)x \tag{8}$$

In the near-field spherical wavefront [47], μ_n is obtained by taking x_n into the near-field distance function, denoted as $\mu_{\mathrm{NL}}(x)$, derived from coordinate operation as

$$\mu_{\mathrm{NL}}(x) = \sqrt{(x - D\cos(\alpha))^2 + (D\sin(\alpha))^2}. \tag{9}$$

B. UPA System Model

The phased UPA Tx is illustrated in Fig. 1(b), with the square UPA positioned along the x-y plane and centered at the origin $O_{\mathrm{P}} = (0,0,0)$. We define the n-th Tx antenna as the antenna at the p-th column and the q-th row, satisfying $n_{p,q} = p + (q-1)\sqrt{N_{\mathrm{T}}}$, where $\{p, q\} = 1, 2, \ldots, \sqrt{N_{\mathrm{T}}}$. The central coordinate of the $n_{p,q}$-th antenna is $C_{n_{p,q}}^{\mathrm{P}} = (x_p, y_q, 0)$, where x_p and y_q are the spatial variables of the UPA, $x_p = \frac{\lambda}{2}(p - \frac{1}{2}) - \frac{L}{2}$, $y_q = \frac{\lambda}{2}(q - \frac{1}{2}) - \frac{L}{2}$, and $L = \frac{\lambda}{2}\sqrt{N_{\mathrm{T}}}$. The coordinate of Rx is given by $C_{\mathrm{Rx}}^{\mathrm{P}} = (D\cos(\alpha_{\mathrm{e}})\cos(\alpha_{\mathrm{a}}), D\cos(\alpha_{\mathrm{e}})\sin(\alpha_{\mathrm{a}}), D\sin(\alpha_{\mathrm{e}}))$, where $\alpha_{\mathrm{e}} \in [-\frac{\pi}{2}, \frac{\pi}{2}]$ and $\alpha_{\mathrm{a}} \in [-\pi, \pi]$ are the elevation and azimuth AoDs, respectively.

The normalized UPA phase shifters, denoted as $\vec{\phi}_{\mathrm{P}}$, corresponding to $n_{p,q} = 1, 2, \ldots, N_{\mathrm{T}}$ Tx antennas, is given by

$$\vec{\phi}_{\mathrm{P}} = \frac{1}{\sqrt{N_{\mathrm{T}}}} \left[e^{j\varphi_{\mathrm{P}}(x_p, y_q)} \right]_{N_{\mathrm{T}} \times 1}, \tag{10}$$

where $\varphi_{\mathrm{P}}(x, y)$ is the UPA spatially dependent phase function that will be designed to achieve maximal throughput.

The equivalent channel gain as a function of f, denoted as $g_{\mathrm{P}}(f)$, is given by

$$g_{\mathrm{P}}(f) = \vec{H}(f)^T \vec{\phi}_{\mathrm{P}}. \tag{11}$$

Similarly, $g_{\mathrm{P}}(f)$ can be expressed in summation form

$$g_{\mathrm{P}}(f) = \sum_{p=1}^{\sqrt{N_{\mathrm{T}}}} \sum_{q=1}^{\sqrt{N_{\mathrm{T}}}} \frac{c e^{j\varphi_{\mathrm{P}}(x_p, y_q)} e^{-j\frac{2\pi f \mu_{n_{p,q}}}{c}}}{4\pi\sqrt{N_{\mathrm{T}}} f \mu_{n_{p,q}}}. \tag{12}$$

In the far-field planar wavefront [47], $\mu_{n_{p,q}}$ is determined by taking x_p and y_q into the far-field UPA distance function, denoted as $\mu_{\mathrm{FP}}(x, y)$

$$\mu_{\mathrm{FP}}(x, y) = D - x\cos(\alpha_{\mathrm{e}})\cos(\alpha_{\mathrm{a}}) - y\cos(\alpha_{\mathrm{e}})\sin(\alpha_{\mathrm{a}}). \tag{13}$$

In the near-field spherical wavefront [47], $\mu_{n_{p,q}}$ is given by taking x_p and y_q into the near-field UPA distance function, denoted as $\mu_{\mathrm{NP}}(x, y)$, derived from coordinate operation as

$$\begin{aligned} \mu_{\mathrm{NP}}(x, y) = [&(D\cos(\alpha_{\mathrm{e}})\cos(\alpha_{\mathrm{a}}) - x)^2 \\ &+ (D\cos(\alpha_{\mathrm{e}})\sin(\alpha_{\mathrm{a}}) - y)^2 + (D\sin(\alpha_{\mathrm{e}}))^2]^{\frac{1}{2}}. \end{aligned} \tag{14}$$

III. Initial Phase Functions

We derive initial phase functions for the ULA and UPA scenarios using the SPM, which achieves uniform power spectrum and provides good initialization for throughput optimization.

A. ULA Scenarios

To apply the SPM, we need to transfer $g_{\mathrm{L}}(f)$ to an integral form, denoted as $\tilde{g}_{\mathrm{L}}(f)$, as the power spectrum is proportional to $|\tilde{g}_{\mathrm{L}}(f)|^2$. We mathematically treat the ULA as continuous, i.e., treat discrete spatial variable x_n as a continuous variable $x \in [-\frac{L}{2}, \frac{L}{2}]$, and μ_n as a continuous function $\mu(x)$. In this way, based on Equation (7), $\tilde{g}_{\mathrm{L}}(f)$ can be formulated as

$$\tilde{g}_{\mathrm{L}}(f) \propto \int_{-\frac{L}{2}}^{\frac{L}{2}} \frac{1}{f\mu(x)} e^{j\varphi_{\mathrm{L}}(x)} e^{-j\frac{2\pi f\mu(x)}{c}} \mathrm{d}x. \tag{15}$$

where the symbol $\propto$ means proportional to. The influence of $\frac{1}{f\mu(x)}$ is very small, and it can be ignored for simplification [38]. We first derive the initial phase function for the far-field ULA scenario, denoted as $\varphi_{\mathrm{FL}}(x)$. By substituting Equation (8) into Equation (15), and applying $\varphi_{\mathrm{FL}}(x)$ for $\varphi_{\mathrm{L}}(x)$, we obtain $|\tilde{g}_{\mathrm{L}}(f)|$ in the far-field scenario

$$|\tilde{g}_{\mathrm{L}}(f)| \propto \left| \int_{-\frac{L}{2}}^{\frac{L}{2}} e^{j\varphi_{\mathrm{FL}}(x)} e^{j\frac{2\pi f}{c} x\cos(\alpha)} \mathrm{d}x \right|. \tag{16}$$

Then, introduce operator $s(x) = -x\cos(\alpha)$, $s \in [s_1, s_2] = \left[-\frac{L}{2}|\cos(\alpha)|, \frac{L}{2}|\cos(\alpha)|\right]$ and operator $\omega(f) = \frac{2\pi f}{c}$, $\omega \in [\omega_1, \omega_2] = [\frac{2\pi}{c}(f_{\mathrm{c}} - \frac{BW}{2}), \frac{2\pi}{c}(f_{\mathrm{c}} + \frac{BW}{2})]$, and define $\psi_{\mathrm{FL}}(s) = \varphi_{\mathrm{FL}}(x(s))$ and $\varrho_{\mathrm{L}}(\omega) = \tilde{g}_{\mathrm{L}}(f(\omega))$, so that Equation (16) becomes

$$|\varrho_{\mathrm{L}}(\omega)| \propto \left| \int_{s_1}^{s_2} e^{j\psi_{\mathrm{FL}}(s)} e^{-j\omega s} \mathrm{d}s \right|, \tag{17}$$

which can be equivalently written in the form of Fourier transform of $\eta_{\mathrm{FL}}(s)$

$$\begin{aligned} &|\varrho_{\mathrm{L}}(\omega)| \propto |\mathcal{F}\{\eta_{\mathrm{FL}}(s)\}|, \\ &\eta_{\mathrm{FL}}(s) = \begin{cases} e^{j\psi_{\mathrm{FL}}(s)}, s \in [s_1, s_2] \\ 0, s \notin [s_1, s_2] \end{cases}. \end{aligned} \tag{18}$$

Thereby, a uniform power spectrum corresponds to uniform $|\varrho_{\mathrm{L}}(\omega)|^2$ in $[\omega_1, \omega_2]$. Now, according to the SPM [48], for a function $f(x) = a(x)e^{j\psi(x)}$, $x \in [x_1, x_2]$, where $a(x)$ represents amplitude, its Fourier transform function $F(\omega) = \mathcal{F}\{f(x)\}$ has approximation

$$|F(\omega)|^2 \approx \frac{2\pi a^2(x)}{|\psi''(x)|} \tag{19}$$

in $\omega \in [\psi'(x_1), \psi'(x_2)]$ if $\psi'(x)$ monotonically increases in $[x_1, x_2]$ [49]. Therefore, to achieve a uniform $|\varrho_{\mathrm{L}}(\omega)|^2$ in $[\omega_1, \omega_2]$, $\psi'_{\mathrm{FL}}(s)$ is assumed to monotonically increases in $[s_1, s_2]$, so that $\psi''_{\mathrm{FL}}(s) > 0, \forall s \in [s_1, s_2]$, and according to Equation (18) and the SPM approximation, $\psi_{\mathrm{FL}}(s)$ needs to satisfy

$$\begin{cases} \psi''_{\mathrm{FL}}(s) \propto 1 \\ \psi'_{\mathrm{FL}}(s_1) = \omega_1 \\ \psi'_{\mathrm{FL}}(s_2) = \omega_2 \end{cases}. \tag{20}$$

Subject to the above conditions, $\psi_{\mathrm{FL}}(s)$ can be solved as

$$\begin{aligned} \psi_{\mathrm{FL}}(s) &= \frac{\omega_2 - \omega_1}{2(s_2 - s_1)} s^2 + \frac{\omega_1 s_2 - \omega_2 s_1}{s_2 - s_1} s + C \\ &= \frac{\pi BW}{cL|\cos(\alpha)|} s^2 + \frac{2\pi f_{\mathrm{c}}}{c} s + C, \end{aligned} \tag{21}$$

where C is a constant and can be eliminated in $|\varrho_{\mathrm{L}}(\omega)|$. Then, $\varphi_{\mathrm{FL}}(x)$ is given by

$$\begin{aligned} \varphi_{\mathrm{FL}}(x) &= \psi_{\mathrm{FL}}(s(x)) \\ &= \frac{\pi BW|\cos(\alpha)|}{cL} x^2 - \frac{2\pi f_{\mathrm{c}}\cos(\alpha)}{c} x. \end{aligned} \tag{22}$$

Similarly, initial phase function for the near-field ULA scenario, denoted as $\varphi_{\mathrm{NL}}(x)$, is derived in Appendix A.

B. UPA Scenarios

To apply the SPM, we need to transfer $g_{\mathrm{P}}(f)$ to an integral form, denoted as $\tilde{g}_{\mathrm{P}}(f)$, by mathematically treating the UPA as continuous, i.e., treating x_p and y_q as continuous variables $\{x, y\} \in [-\frac{L}{2}, \frac{L}{2}]$, and $\mu_{n_{p,q}}$ as a continuous bivariable function $\mu(x, y)$. Based on Equation (12) and ignoring the amplitude, $\tilde{g}_{\mathrm{P}}(f)$ is given by

$$\tilde{g}_{\mathrm{P}}(f) \propto \int_{-\frac{L}{2}}^{\frac{L}{2}} \int_{\frac{L}{2}}^{\frac{L}{2}} e^{j\varphi_{\mathrm{P}}(x,y)} e^{-j\frac{2\pi f\mu(x,y)}{c}} \mathrm{d}x\mathrm{d}y. \tag{23}$$

We first derive the initial phase function for the far-field UPA scenario, denoted as $\varphi_{\mathrm{FP}}(x, y)$. The difficulty is that the spatial bivariable $\{x, y\}$ introduces a double integral in $\tilde{g}_{\mathrm{P}}(f)$. Therefore, we need to isolate the impact of x and y on $\tilde{g}_{\mathrm{P}}(f)$. By substituting Equation (13) into Equation (23), we obtain $\tilde{g}_{\mathrm{P}}(f)$ in the far-field scenario

$$\begin{aligned} |\tilde{g}_{\mathrm{P}}(f)| \propto &\int_{-\frac{L}{2}}^{\frac{L}{2}} \int_{-\frac{L}{2}}^{\frac{L}{2}} e^{j\varphi_{\mathrm{FP}}(x,y)} \times \\ &e^{j\frac{2\pi f}{c}(x\cos(\alpha_{\mathrm{e}})\cos(\alpha_{\mathrm{a}}) + y\cos(\alpha_{\mathrm{e}})\sin(\alpha_{\mathrm{a}}) - D)} \mathrm{d}x\mathrm{d}y. \end{aligned} \tag{24}$$

Then, we assume $\varphi_{\mathrm{FP}}(x, y)$ is constructed by $\varphi_{\mathrm{x}}(x)$ and $\varphi_{\mathrm{y}}(y)$

$$\varphi_{\mathrm{FP}}(x, y) = \varphi_{\mathrm{x}}(x) + \varphi_{\mathrm{y}}(y). \tag{25}$$

Although the assumption constrains the structure of $\varphi_{\mathrm{FP}}(x, y)$, it makes $\tilde{g}_{\mathrm{P}}(f)$ disassembled into $g_{\mathrm{x}}(f)$ and $g_{\mathrm{y}}(f)$

$$\tilde{g}_{\mathrm{P}}(f) \propto g_{\mathrm{x}}(f) g_{\mathrm{y}}(f) e^{-j\frac{2\pi f}{c} D}, \tag{26}$$

$$g_{\mathrm{x}}(f) = \int_{-\frac{L}{2}}^{\frac{L}{2}} e^{j\varphi_{\mathrm{x}}(x)} e^{j\frac{2\pi f}{c} x\cos(\alpha_{\mathrm{e}})\cos(\alpha_{\mathrm{a}})} \mathrm{d}x, \tag{27}$$

$$g_{\mathrm{y}}(f) = \int_{-\frac{L}{2}}^{\frac{L}{2}} e^{j\varphi_{\mathrm{y}}(y)} e^{j\frac{2\pi f}{c} y\cos(\alpha_{\mathrm{e}})\sin(\alpha_{\mathrm{a}})} \mathrm{d}y. \tag{28}$$

To obtain uniform $|\tilde{g}_{\mathrm{P}}(f)|^2$, both $|g_{\mathrm{x}}(f)|^2$ and $|g_{\mathrm{y}}(f)|^2$ must be uniform, which can be achieved by designing $\varphi_{\mathrm{x}}(x)$ and $\varphi_{\mathrm{y}}(y)$ using the SPM as in Section III-A. Accordingly, letting $\cos(\alpha_{\mathrm{x}}) = \cos(\alpha_{\mathrm{e}})\cos(\alpha_{\mathrm{a}})$ and $\cos(\alpha_{\mathrm{y}}) = \cos(\alpha_{\mathrm{e}})\sin(\alpha_{\mathrm{a}})$, $\varphi_{\mathrm{x}}(x)$ and $\varphi_{\mathrm{y}}(y)$ are given by

$$\varphi_{\mathrm{x}}(x) = \frac{\pi BW|\cos(\alpha_{\mathrm{x}})|}{cL} x^2 - \frac{2\pi f_{\mathrm{c}}\cos(\alpha_{\mathrm{x}})}{c} x, \tag{29}$$

$$\varphi_{\mathrm{y}}(y)=\frac{\pi BW|\cos(\alpha_{\mathrm{y}})|}{cL}y^2-\frac{2\pi f_{\mathrm{c}}\cos(\alpha_{\mathrm{y}})}{c}y. \tag{30}$$

Then, $\varphi_{\mathrm{FP}}(x,y)$ is derived by Equation (25)

$$\begin{aligned}\varphi_{\mathrm{FP}}(x,y)=&\frac{\pi BW}{cL}(|\cos(\alpha_{\mathrm{x}})|\,x^2+|\cos(\alpha_{\mathrm{y}})|\,y^2)\\&-\frac{2\pi f_{\mathrm{c}}}{c}(\cos(\alpha_{\mathrm{x}})x+\cos(\alpha_{\mathrm{y}})y).\end{aligned} \tag{31}$$

However, for the near-field scenario, according to $\mu_{\mathrm{NP}}(x,y)$ in Equation (14), $\tilde{g}_{\mathrm{P}}(f)$ cannot be disassembled and the SPM is not applicable directly. But to merely obtain initial phase function, we can apply relaxation, i.e., replace $\mu_{\mathrm{NP}}(x,y)$ by its closest expression, denoted as $\tilde{\mu}_{\mathrm{NP}}(x,y)$, in form of

$$\tilde{\mu}_{\mathrm{NP}}(x,y)=k_0+k_1x+k_2x^2+k_3y+k_4y^2, \tag{32}$$

where coefficients k_0 to k_4 are determined by the least square method (LSM) between $\mu_{\mathrm{NP}}(x,y)$ and $\tilde{\mu}_{\mathrm{NP}}(x,y)$. In this way, $\tilde{g}_{\mathrm{P}}(f)$ can be disassembled and a closed-form solution is derivable. Initial phase function for the near-field UPA scenario, denoted as $\varphi_{\mathrm{NP}}(x,y)$, is derived in Appendix B.

IV. Optimization Method

The initial phase functions cannot guarantee optimal throughput. We formulate the throughput optimization problem and present optimal phase functions by polynomials. To obtain maximal throughput, we develop an gradient descent-based algorithm initialized with the initial phase functions

A. Optimization for ULA Scenarios

We maximize throughput (TP) via optimal phase function, where TP depends on signal-to-noise ratio (SNR) [50]

$$TP=\frac{BW}{S_{\mathrm{c}}}\sum_{m=1}^{S_{\mathrm{c}}}\log_2(1+SNR(f_m)), \tag{33}$$

$$SNR(f_m)=\frac{\rho_{\mathrm{t}}}{S_{\mathrm{c}}\rho_{\mathrm{r}}(f_m)}|g_{\mathrm{L}}(f_m)|^2, \tag{34}$$

where ρ_{t} is input power, $\rho_{\mathrm{r}}(f_m)$ is received noise power that $\rho_{\mathrm{r}}(f_m)=\frac{BW}{S_{\mathrm{c}}}PSD(f_m)$ and $PSD(f_m)$ is the thermal noise power spectral density at f_m [50]. According to Equation (7), $SNR(f_m)$ can be further expressed as

$$SNR(f_m)=\frac{\rho_{\mathrm{t}}}{N_{\mathrm{T}}S_{\mathrm{c}}\rho_{\mathrm{r}}(f_m)}\left|\sum_{n=1}^{N_{\mathrm{T}}}e^{j\varphi_{\mathrm{L}}(x_n)}h_n(f_m)\right|^2. \tag{35}$$

Since TP depends on $\varphi_{\mathrm{L}}(x)$, the optimization problem is

$$\hat{\varphi}_{\mathrm{L}}(x)=\max_{\varphi_{\mathrm{L}}(x)}\arg\, TP(\varphi_{\mathrm{L}}(x)). \tag{36}$$

where $\hat{\varphi}_{\mathrm{L}}(x)$ is optimal phase function for ULA. To make the problem resolvable, we represent $\varphi_{\mathrm{L}}(x)$ as polynomial

$$\varphi_{\mathrm{L}}(x)=\sum_{t=1}^{T}\varepsilon_t x^t, \tag{37}$$

with degree T and coefficients ε_t. The finite domain $x\in[\frac{-L}{2},\frac{L}{2}]$ enables effective finite polynomial representation. Next, we optimize $\vec{\varepsilon}=[\varepsilon_t]_{T\times1}$ to maximize TP

$$\vec{\varepsilon}_{\mathrm{o}}=\max_{\vec{\varepsilon}}\arg\, TP, \tag{38}$$

where $\vec{\varepsilon}_{\mathrm{o}}$ is optimal coefficients.

We design an iterative algorithm based on gradient descent to solve the maximization problem in (38). The gradients of TP with respect to $\vec{\varepsilon}$ at the i-th ($i=1,2,\cdots,I$) is denoted as $\nabla_{\vec{\varepsilon}}TP[i]$. For the next iteration, $\vec{\varepsilon}$ is given by

$$\vec{\varepsilon}[i+1]=\vec{\varepsilon}[i]+\mathrm{sign}\{\nabla_{\vec{\varepsilon}}TP[i]\}\odot\vec{S}[i], \tag{39}$$

where $\mathrm{sign}\{\cdot\}$ is the pointwise sign function that $\mathrm{sign}\{x\}=\frac{x}{|x|}$, $\odot$ is the pointwise multiplication and $\vec{S}$ is the step-length vector that $\vec{S}=[S_t]_{T\times1}$. In this way, ε_t always tracks the positive direction of the t-th gradient at different iterations.

To accelerate convergence, we design $\vec{S}$ as adaptive that when $i>1$, $S_t[i]$ will stretch by a factor σ if the t-th gradient keeps the same sign compared to the last iteration, or shrink to half if not. That is

$$\begin{cases}S_t[i]=\sigma S_t[i-1],\Gamma_t[i]>0\\S_t[i]=\frac{1}{2}S_t[i-1],\Gamma_t[i]\le0\end{cases}, \tag{40}$$

where $[\Gamma_t[i]]_{T\times1}=\nabla_{\vec{\varepsilon}}TP[i]\odot\nabla_{\vec{\varepsilon}}TP[i-1]$. When $i=1$, just set $\vec{S}[1]=[1]_{T\times1}$. Moreover, convergence can be adjusted by changing σ. In order to achieve fast and steady convergence, σ is usually set slightly less than 2, which will be discussed further in Section IV-C.

With these settings, the step-length will continuously stretch when the direction of the gradient remains unchanged during the tracking. When the direction inverts, indicating that the maximum value occurs between the last two steps, the step-length will be halved to approach it. When it comes to the optima where the direction of gradients will frequently change, the step-length will be zeroed since $\sigma<2$, ensuring convergence for the algorithm. Besides, the accumulation of step-length can achieve an effect similar to the momentum gradient ascent method. This makes the changes of partial gradients have limited impact on the overall search direction, effectively avoiding iterations from falling into local optima.

For the far-field scenario, we initialize $\vec{\varepsilon}$ based on the initial phase function $\varphi_{\mathrm{FL}}(x)$ in Equation (22) by setting

$$\vec{\varepsilon}[1]=\begin{bmatrix}-\frac{2\pi f_{\mathrm{c}}\cos(\alpha)}{c}\\\frac{\pi BW|\cos(\alpha)|}{cL}\\[0]_{(T-2)\times1}\end{bmatrix}_{T\times1}, \tag{41}$$

and for the near-field scenario, we initialize $\vec{\varepsilon}$ by using the LSM between $\varphi_{\mathrm{L}}(x)$ and $\varphi_{\mathrm{NL}}(x)$. Thus, optimization starts from the initial phase functions and the distance to optima is shortened. The algorithm can be applied to either far or near-field scenario by calculating $h_n(f_m)$ using $\mu_{\mathrm{FL}}(x_n)$ in Equation (8) or $\mu_{\mathrm{NL}}(x_n)$ in Equation (9), respectively.

B. Optimization for UPA Scenarios

Similarly, the optimal UPA phase function, denoted as $\hat{\varphi}_{\mathrm{P}}(x,y)$, is obtained by maximizing TP where $SNR(f_m)$ is now given by $g_{\mathrm{P}}(f_m)$

$$\begin{aligned}SNR(f_m)&=\frac{\rho_{\mathrm{t}}}{S_{\mathrm{c}}\rho_{\mathrm{r}}(f_m)}|g_P(f_m)|^2\\&=\frac{\rho_{\mathrm{t}}}{N_{\mathrm{T}}S_{\mathrm{c}}\rho_{\mathrm{r}}(f_m)}\left|\sum_{p=1}^{\sqrt{N_{\mathrm{T}}}}\sum_{q=1}^{\sqrt{N_{\mathrm{T}}}}e^{j\varphi_{\mathrm{P}}(x_p,y_q)}h_{n_{p,q}}(f_m)\right|^2.\end{aligned} \tag{42}$$

Algorithm 1: Optimization of phase shifters

Input: T, I, σ, L, f_{c}, c, BW, D, α, α_{x}, α_{y}
Output: $\vec{\phi}_{\mathrm{L}}$ or $\vec{\phi}_{\mathrm{P}}$

```
Set S⃗[1] = [1]_{T×1} or [1]_{(T²+3T)/2×1} for ULA or UPA;
Initialize ε⃗[1] based on φ_FL, φ_NL, φ_FP, or φ_NP for far or near-field ULA or UPA;
Calculate μ_n by Equation (8), (9), (13), or (14) for far or near-field ULA or UPA;
Calculate h_n(f_m) by Equation (2);
Set i = 1;
while i ≤ I do
    Calculate φ_L(x_n)[i] or φ_P(x_p, y_q)[i] by Equation (37) or (43) for ULA or UPA;
    Calculate SNR(f_m)[i] by Equation (35) or (42) for ULA or UPA;
    Calculate TP[i] by Equation (33) and ∇_ε⃗ TP[i];
    if i > 1 then
        Update S⃗[i] by Equation (40);
    end
    if i < I then
        i = i + 1;
        Update ε⃗[i] by Equation (39);
    end
end
Calculate φ⃗_L or φ⃗_P by Equation (5) or (10) using φ_L(x_n)[I] or φ_P(x_p, y_q)[I] for ULA or UPA;
```

In this scenario, we need to present the bivariable phase function $\varphi_{\mathrm{P}}(x,y)$ by a new polynomial expansion

$$\varphi_{\mathrm{P}}(x,y)=\sum_{u=1}^{T}\sum_{v=0}^{u}\varepsilon_{t_{u,v}}x^{u-v}y^{v}, \tag{43}$$

where $\varepsilon_{t_{u,v}}$ is the coefficient of the $t_{u,v}$-th term and $t_{u,v}=\frac{u^2+u}{2}+v$. The total terms is given by $\max(t_{u,v})=\frac{T^2+3T}{2}$. In the same way, maximal TP and $\hat{\varphi}_{\mathrm{P}}(x,y)$ can be achieved by optimizing $\vec{\varepsilon}$ as in Equation (38).

The algorithm is similar to the ULA scenario. For the far-field scenario, $\vec{\varepsilon}$ is initialized based on the initial phase function $\varphi_{\mathrm{FP}}(x,y)$ in Equation (31) by setting

$$\vec{\varepsilon}[1]=\begin{bmatrix} -\frac{2\pi f_{\mathrm{c}}}{c}\cos(\alpha_{\mathrm{x}}) \\ -\frac{2\pi f_{\mathrm{c}}}{c}\cos(\alpha_{\mathrm{y}}) \\ \frac{\pi BW}{cL}|\cos(\alpha_{\mathrm{x}})| \\ 0 \\ \frac{\pi BW}{cL}|\cos(\alpha_{\mathrm{y}})| \\ [0]_{(\frac{T^2+3T}{2}-5)\times 1} \end{bmatrix}_{\frac{T^2+3T}{2}\times 1}. \tag{44}$$

For the near-field scenario, $\vec{\varepsilon}$ is initialized by using the LSM between $\varphi_{\mathrm{P}}(x,y)$ and $\varphi_{\mathrm{NP}}(x,y)$. To apply to the far or near-field scenario, calculate $h_{n_{p,q}}(f_m)$ using $\mu_{\mathrm{FP}}(x_p,y_q)$ in Equation (13) or $\mu_{\mathrm{NP}}(x_p,y_q)$ in Equation (14), respectively. The complete optimization process is outlined in Algorithm 1, where I is the iteration limit.

C. Recommended Values of Parameters

In this section, we provide recommended values of the parameters T, I and σ by analyzing simulation-based performance of the optimization algorithm based on simulations. We consider $f_{\mathrm{c}}=300\,\mathrm{GHz}$, $BW=30\,\mathrm{GHz}$, and $S_{\mathrm{c}}=256$. We set $N_{\mathrm{T}}=64$ for the ULA and $N_{\mathrm{T}}=64\times 64$ for the UPA. Thus, $L=32\,\mathrm{mm}$ and $D_{\mathrm{R}}=2.048\,\mathrm{m}$. Therefore, we use $D=5\,\mathrm{m}$ and $D=0.5\,\mathrm{m}$ for the far-field and near-field scenarios, respectively. We assume $\rho_{\mathrm{t}}=30\,\mathrm{dBm}$ in far-field transmission and $\rho_{\mathrm{t}}=10\,\mathrm{dBm}$ in near-field transmission. $PSD(f_m)$ is calculated at room temperature of $17\,^{\circ}\mathrm{C}$ [50]. The phase shifters are considered to have infinite phase resolution. Each result is the average of 3000 randomly generated Rx.

The parameter T determines the degree of the polynomial, as well as the number of coefficients to be optimized. Theoretically, the optimal phase function can be approximated more accurately with a larger T, but it will also lead to greater computational complexity. To illustrate the influence of T on the optimization, Fig. 2 shows throughput at different iterations with various values of T. For the ULA scenarios in Fig. 2(a), there is a significant gap between throughput achieved with $T=3$ and $T=4$, indicating that $T<4$ is insufficient for the optimization. However, the effect of increasing T beyond 4 on the maximization is negligible, but will result in higher complexity. The same trend can be observed in the UPA scenarios as shown in Fig. 2(b).

We also conduct simulations for extremely large ULA scenario with $N_{\mathrm{T}}=1024$ and extremely wide bandwidth UPA scenario with $BW=100\,\mathrm{GHz}$. The convergences of throughput for these two examples are shown in Fig. 3. For the extremely-large ULA scenario in Fig. 3(a), though the differences in throughput between $T=4$, $T=5$, and $T=6$ have slightly enlarged compared with that in Fig. 2(a), $T=4$ is still acceptable for achieving the optimal trade-off between throughput performance and computational cost. For the extremely-wideband UPA scenario in Fig. 3(b), the effect of applying T beyond 4 remains negligible. Through the above results, it indicates that $T=4$ possesses considerable applicability, thus we recommend this value in the proposed optimization algorithm.

To present the influence of σ on the optimization, Fig. 4 plots throughput at different iterations with various values of σ. It shows that in the preliminary stage of maximization, a larger σ results in faster convergence, as it corresponds to a greater stretch of step-length. However, for $\sigma=2$, the convergence becomes unstable afterward, leading to oscillations that diminish the effectiveness of maximization. For $\sigma<1.8$, the convergence will be slower, and more iterations, as well as higher computational cost, is needed to reach the optima. Hence, we recommend $\sigma=1.8$. In all the scenarios, with $\sigma=1.8$, throughput can be considered fully maximized after about 150 iterations. Therefore, $I=150$ is recommended.

V. Simulation Results

We present simulation results including power spectrum, throughput, BER, and various robustness tests. We evaluate initial phase functions (φ_{FL}, φ_{NL}, φ_{FP}, φ_{NP}) and

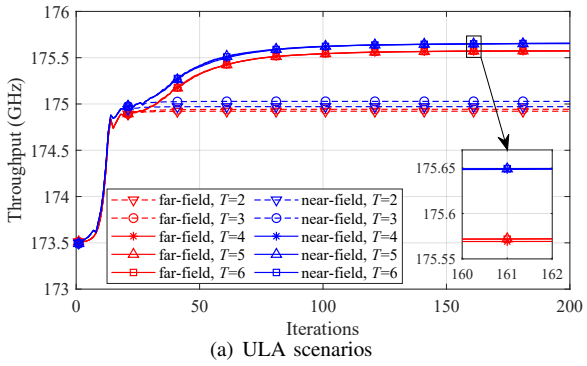

(a) ULA scenarios

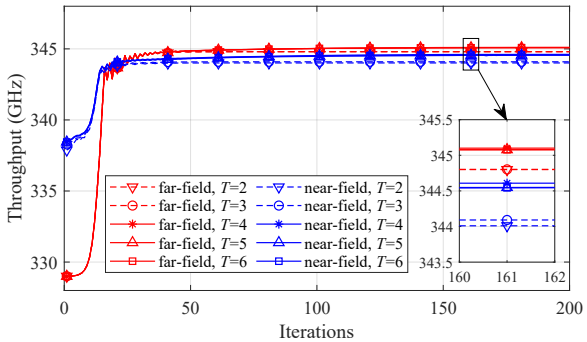

(b) UPA scenarios

Fig. 2. Convergence of TP varying with T, where $\sigma = 1.8$ and $I = 200$.

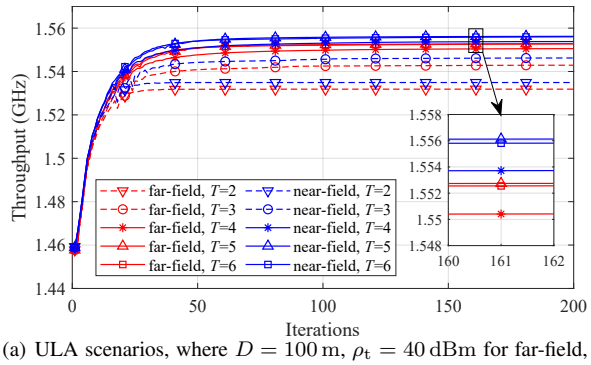

(a) ULA scenarios, where $D = 100\,\text{m}$, $\rho_\text{t} = 40\,\text{dBm}$ for far-field, and $D = 1\,\text{km}$, $\rho_\text{t} = 20\,\text{dBm}$ for near-field

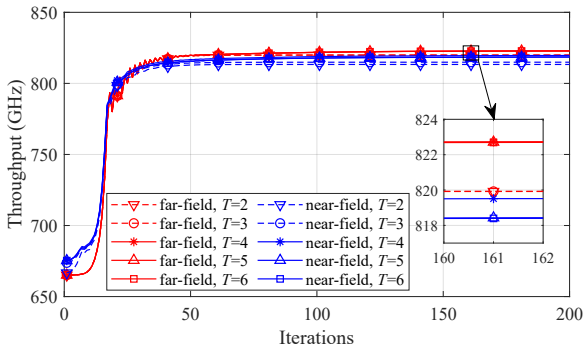

(b) UPA scenarios

Fig. 3. Convergence of TP varying with T in ULA scenario with extremely large array ($N_\text{T} = 1024$) (a) and UPA scenario with extremely wide bandwidth ($BW = 100\,\text{GHz}$) (b).

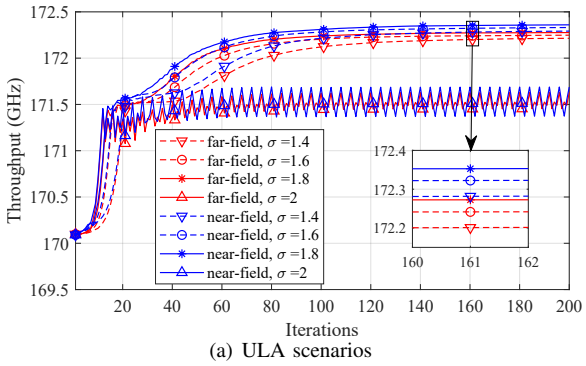

(a) ULA scenarios

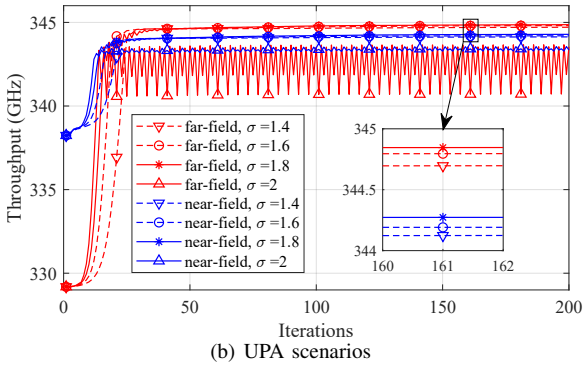

(b) UPA scenarios

Fig. 4. Convergence of TP varying with σ, where $T = 4$, and $I = 200$.

optimal phase functions ($\hat{\varphi}_\text{L}$, $\hat{\varphi}_\text{P}$) using IV-C conditions. The simulations are performed by MATLAB R2022b on an Intel(R) Core(TM) i7-10510U CPU at 1.80 GHz with a 16.0 GB RAM. We simulate BER under QPSK modulation ($M = 4$) using MATLAB's function $BER(f_m) =$ berawgn($R_\text{bn}(f_m)$, 'psk', M, 'nondiff') with energy-per-bit to noise ratio $R_\text{bn}(f_m) = 10\lg(\frac{SNR(f_m)}{\log_2(M)})$. BER is given by the average value of $BER(f_m)$ at every f_m.

We compare against conventional narrowband beamforming [15] (baseline), and state-of-the-art SVD-based [40], and VSA-based [31] wideband beamforming methods. The baseline uses AoD steering vectors without UWB adaptation. For the SVD-based method, the required information is the THz UWB channel $\vec{H}(f_m)$. For the VSA-based method, all AoD, f_c, BW, and N_T are needed, where f_c and BW are adjusted for THz UWB scenarios.

A. Results for the ULA Scenarios

To demonstrate the effect of the proposed solutions on the received signal power spectrum, Fig. 5 shows the value of $|g_\text{L}(f)|^2$ across the frequency band for the far-field and near-field ULA scenarios. As shown in Figs. 5(a) and Fig. 5(b), the initial phase functions provide more uniform $|g_\text{L}(f)|^2$ than the baselines as they are designed using the SPM, while the optimal phase functions has better anti-fading effect near the band edges than the initial ones. This result indicates that the purpose of designing the initial phase functions has been effectively achieved, and the optimal phase functions yield the best effect in making the received signal power more uniform.

Moreover, to illustrate the different impact on beamforming between THz and mmWave scenarios and highlight the pertinence of the proposed method in THz UWB communications, we also simulate $|g_\text{L}(f)|^2$ in mmWave scenario for

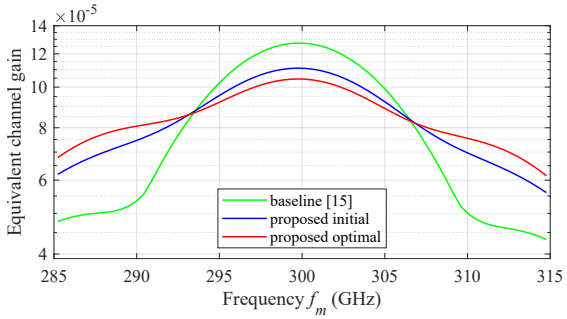

(a) Far-field scenario with $\varphi_{\mathrm{FL}}(x)$ and $\hat{\varphi}_{\mathrm{L}}(x)$

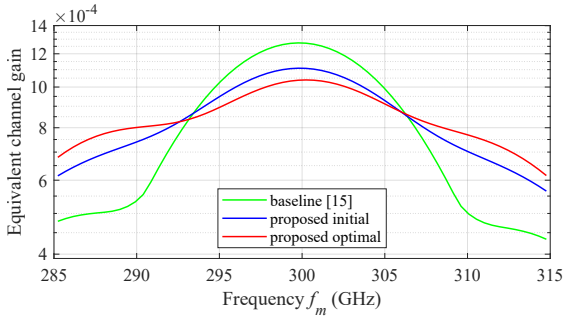

(b) Near-field scenario with $\varphi_{\mathrm{NL}}(x)$ and $\hat{\varphi}_{\mathrm{L}}(x)$

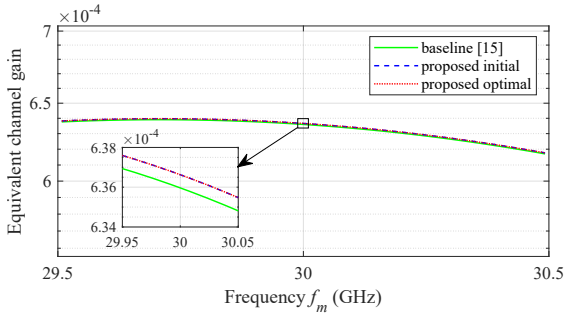

(c) Far-field scenario under mmWave condition ($f_{\mathrm{c}} = 30\,\mathrm{GHz}$, $BW = 1\,\mathrm{GHz}$, and $N_{\mathrm{T}} = 16$)

Fig. 5. Spectrum of $|g_{\mathrm{L}}(f_m)|^2$ in the ULA scenarios.

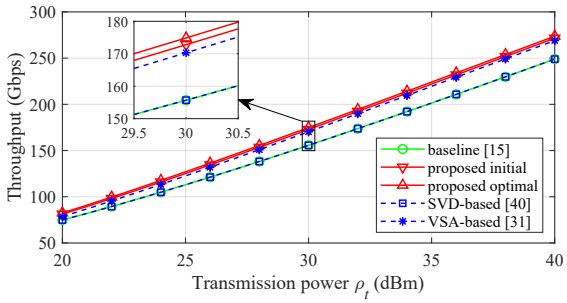

(a) Far-field scenario with $\varphi_{\mathrm{FL}}(x)$ and $\hat{\varphi}_{\mathrm{L}}(x)$

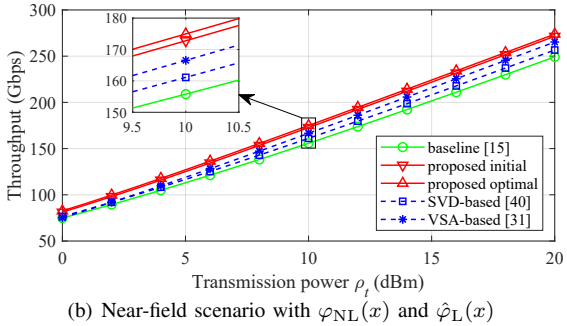

(b) Near-field scenario with $\varphi_{\mathrm{NL}}(x)$ and $\hat{\varphi}_{\mathrm{L}}(x)$

Fig. 6. TP versus transmission power ρ_{t} in the ULA scenarios.

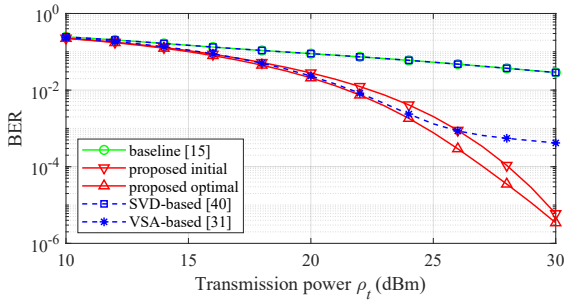

(a) Far-field scenario with $\varphi_{\mathrm{FL}}(x)$ and $\hat{\varphi}_{\mathrm{L}}(x)$

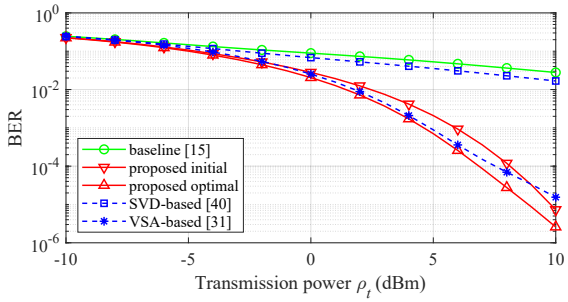

(b) Near-field scenario with $\varphi_{\mathrm{NL}}(x)$ and $\hat{\varphi}_{\mathrm{L}}(x)$

Fig. 7. BER versus transmission power ρ_{t} in the ULA scenarios.

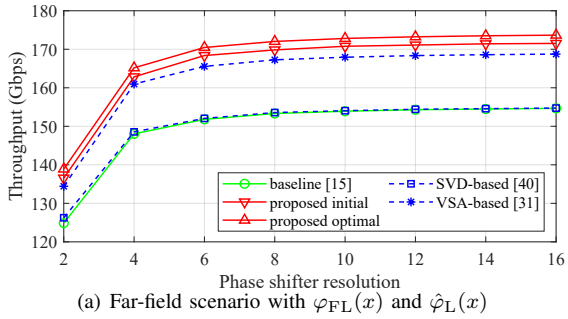

(a) Far-field scenario with $\varphi_{\mathrm{FL}}(x)$ and $\hat{\varphi}_{\mathrm{L}}(x)$

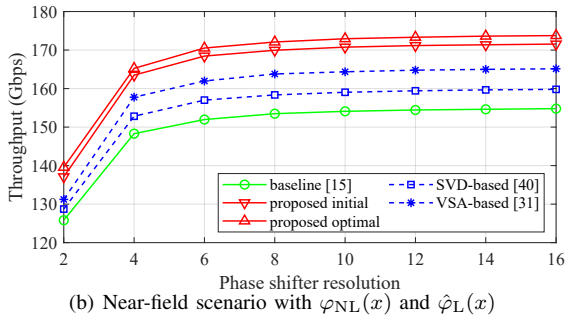

(b) Near-field scenario with $\varphi_{\mathrm{NL}}(x)$ and $\hat{\varphi}_{\mathrm{L}}(x)$

Fig. 8. TP versus phase resolution in the ULA scenarios.

comparison. By taking far-field scenario as an example (since far-field is usually considered in mmWave), Fig. 5(c) presents the gain spectrum in mmWave setup with $f_{\mathrm{c}} = 30\,\mathrm{GHz}$, $BW = 1\,\mathrm{GHz}$, and $N_{\mathrm{T}} = 16$. As shown, even for the baseline, $|g_{\mathrm{L}}(f)|^2$ has a much more uniform curvature than that in THz scenario shown in Fig. 5(a). The improvement made by the proposed initial and optimal phase functions is very limited. This indicates that the beam splitting effect is significantly weaker in mmWave (thus be regarded as beam squint), and the proposed method is more efficient and targeted for THz UWB scenario.

Uniformed received signal power is insufficient to guarantee the performance in terms of throughput or BER. Thus, Fig. 6 shows the throughput versus transmission power for

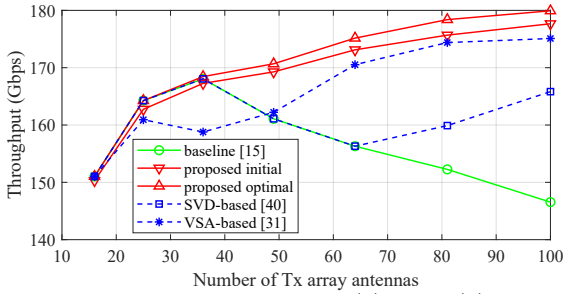

(a) Far-field scenario with $\varphi_{\mathrm{FL}}(x)$ and $\hat{\varphi}_{\mathrm{L}}(x)$

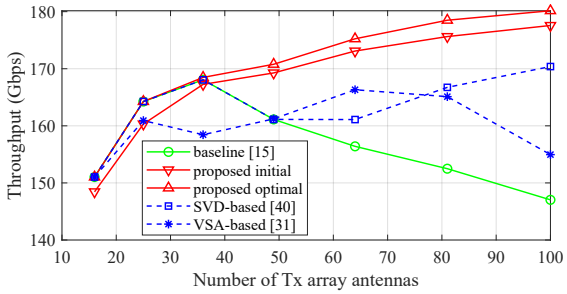

(b) Near-field scenario with $\varphi_{\mathrm{NL}}(x)$ and $\hat{\varphi}_{\mathrm{L}}(x)$

Fig. 9. TP versus Tx antenna number N_{T} in the ULA scenarios.

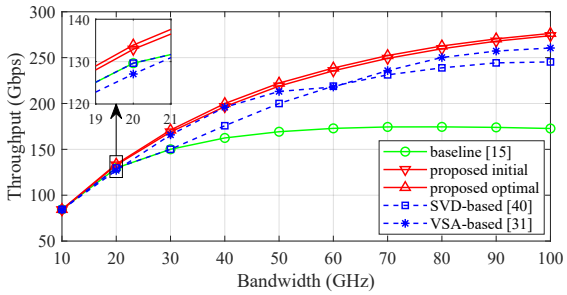

(a) Far-field scenario with $\varphi_{\mathrm{FL}}(x)$ and $\hat{\varphi}_{\mathrm{L}}(x)$

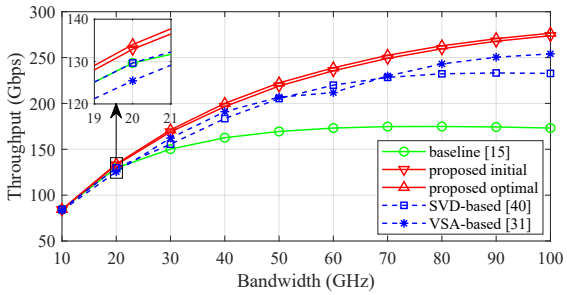

(b) Near-field scenario with $\varphi_{\mathrm{NL}}(x)$ and $\hat{\varphi}_{\mathrm{L}}(x)$

Fig. 10. TP versus bandwidth in the ULA scenarios.

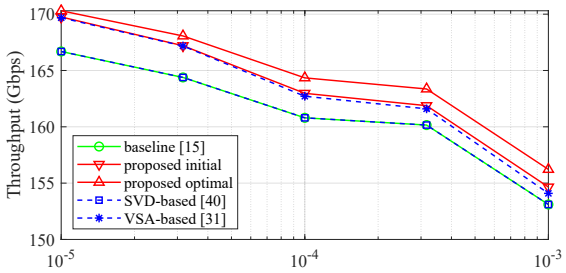

(a) Far-field scenario with $\varphi_{\mathrm{FL}}(x)$ and $\hat{\varphi}_{\mathrm{L}}(x)$

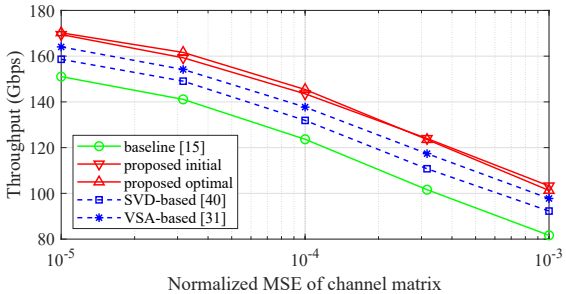

(b) Near-field scenario with $\varphi_{\mathrm{NL}}(x)$ and $\hat{\varphi}_{\mathrm{L}}(x)$

Fig. 11. TP versus MSE of channel $\vec{H}(f_m)$ in the ULA scenarios.

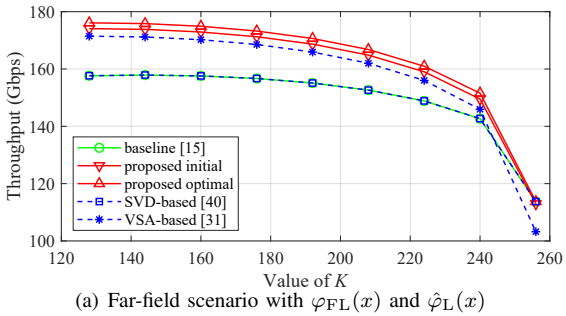

(a) Far-field scenario with $\varphi_{\mathrm{FL}}(x)$ and $\hat{\varphi}_{\mathrm{L}}(x)$

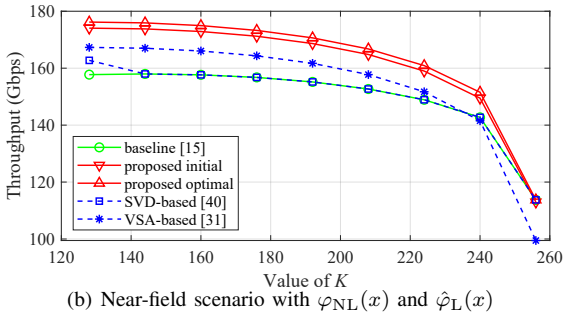

(b) Near-field scenario with $\varphi_{\mathrm{NL}}(x)$ and $\hat{\varphi}_{\mathrm{L}}(x)$

Fig. 12. TP versus number of middle band subcarriers K for non-uniform subcarrier allocation in the ULA scenarios.

the proposed method and existing alternatives, while Fig. 7 compares their BER. From these figures, it is clear that the proposed optimal phase functions provide the highest throughput and significantly reduced BER, validating the effectiveness of the proposed optimization algorithm. These results evidently demonstrate the advantage of the proposed analog beamforming method.

To verify the applicability of the proposed method in real-world phased array systems, Fig. 8 presents throughput with respect to finite phase resolution where the phase has uniform quantization in the range of $[-\pi, \pi]$. The figure shows that the proposed solutions consistently achieve higher throughput compared with other methods even in the low-resolution case, demonstrating their effectiveness in practical applications.

Furthermore, to test the robustness of our method, we evaluate the throughput with varying number of Tx antennas N_{T}, the bandwidth BW, and different channel estimation error (MSE). The results are shown in Fig. 9, Fig. 10, and Fig. 11, respectively. In Fig. 9, the throughput of the proposed optimal phase functions for both far-field and near-field scenarios constantly maintains its top position at different values of N_{T}. The advantage of the proposed solutions can also be observed in Fig. 10, it is clear that with the increase in bandwidth, the proposed solutions achieve a more significant improvement in throughput compared to the baseline. This also corroborates the effectiveness of the proposed method for UWB scenarios. As shown in Fig. 11, although all the methods exhibit a decline in throughput as MSE increases, the proposed

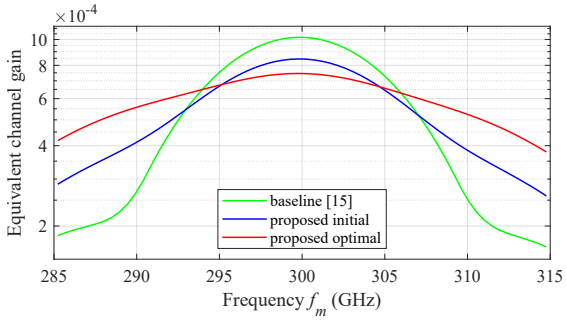

(a) Far-field scenario with $\varphi_{\mathrm{FP}}(x)$ and $\hat{\varphi}_{\mathrm{P}}(x)$

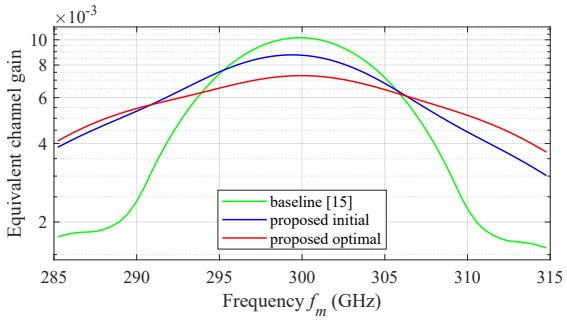

(b) Near-field scenario with $\varphi_{\mathrm{NP}}(x)$ and $\hat{\varphi}_{\mathrm{P}}(x)$

Fig. 13. Spectrum of $|g_{\mathrm{P}}(f_m)|^2$ in the UPA scenarios.

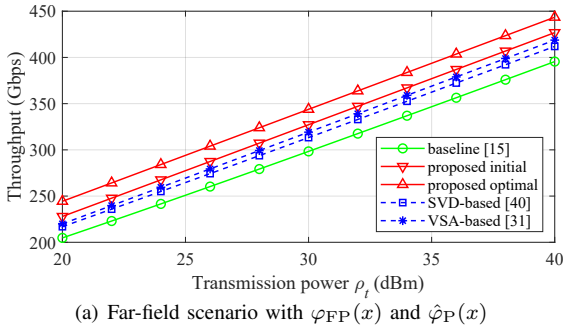

(a) Far-field scenario with $\varphi_{\mathrm{FP}}(x)$ and $\hat{\varphi}_{\mathrm{P}}(x)$

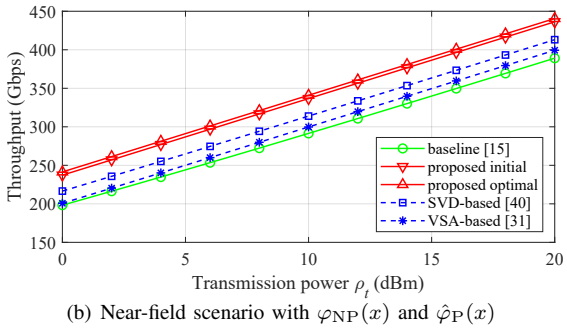

(b) Near-field scenario with $\varphi_{\mathrm{NP}}(x)$ and $\hat{\varphi}_{\mathrm{P}}(x)$

Fig. 14. TP versus transmission power ρ_{t} in the UPA scenarios.

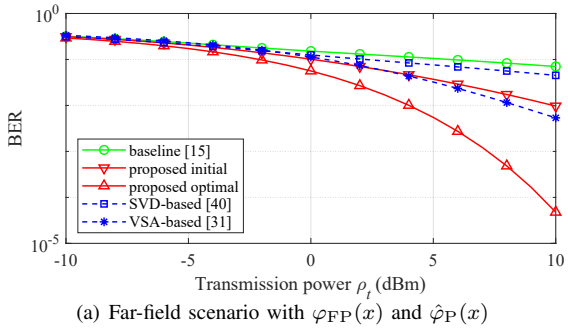

(a) Far-field scenario with $\varphi_{\mathrm{FP}}(x)$ and $\hat{\varphi}_{\mathrm{P}}(x)$

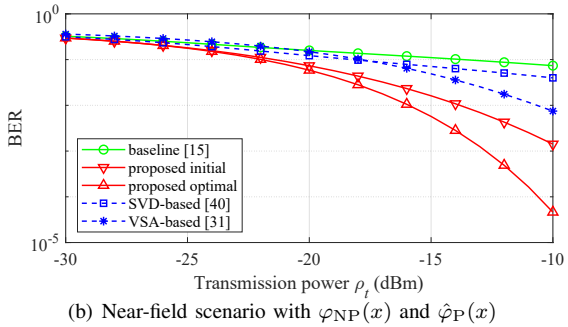

(b) Near-field scenario with $\varphi_{\mathrm{NP}}(x)$ and $\hat{\varphi}_{\mathrm{P}}(x)$

Fig. 15. BER versus transmission power ρ_{t} in the UPA scenarios.

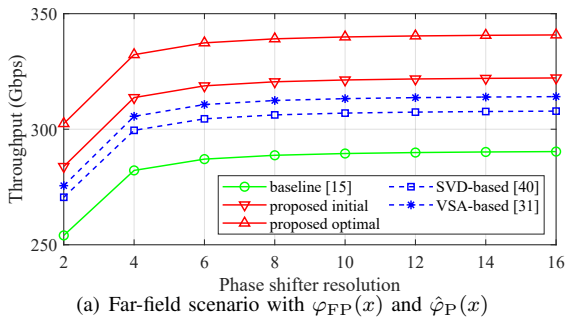

(a) Far-field scenario with $\varphi_{\mathrm{FP}}(x)$ and $\hat{\varphi}_{\mathrm{P}}(x)$

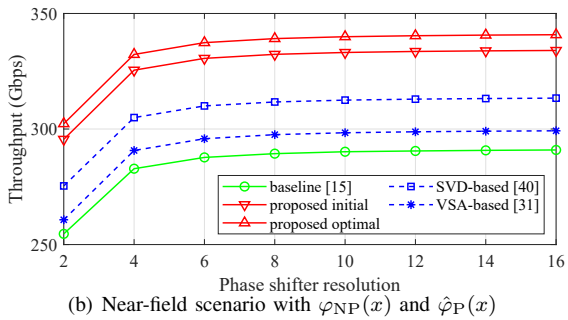

(b) Near-field scenario with $\varphi_{\mathrm{NP}}(x)$ and $\hat{\varphi}_{\mathrm{P}}(x)$

Fig. 16. TP versus phase resolution in the UPA scenarios.

solutions provide the highest throughput in both far-field and near-field scenarios. From the above results, it can be seen that the proposed method exhibits robustness under different conditions with the ULA configuration.

Moreover, some THz systems may use non-uniform subcarrier allocations. Though our initial phase functions are not designed for that, the optimal phase functions can have certain adaptability since non-uniform subcarrier channels are involved in the optimization process. To explore the performance of the proposed method in such case, we defined a non-uniform subcarrier set where K ($\frac{S_{\mathrm{c}}}{2} \leq K \leq S_{\mathrm{c}}$) subcarriers are evenly allocated in half of the bandwidth centered at f_{c}. That is, K subcarriers are in the middle band $[f_{\mathrm{c}} - \frac{BW}{4}, f_{\mathrm{c}} + \frac{BW}{4}]$, and the rest $S_{\mathrm{c}} - K$ subcarriers are in the outer band $[f_{\mathrm{c}} - \frac{BW}{2}, f_{\mathrm{c}} - \frac{BW}{4}) \cup (f_{\mathrm{c}} + \frac{BW}{4}, f_{\mathrm{c}} + \frac{BW}{2}]$. In this way, higher the value of K, denser the allocation in the middle band. We define this pattern under the consideration that denser allocation is usually used in bands with better channel conditions, and in our case, higher channel gain occurs in the middle band. Afterwards, we simulate throughput varying with K, and the result is presented in Fig. 12. As shown, for all the methods in both scenarios, throughput decreases as K increases. When $K = S_{\mathrm{c}}$, which means all the subcarriers are in the middle band and effective bandwidth is cut to half, throughput experiences a quick drop. This result is in line with Fig. 10, where throughput is reduced as bandwidth decreases.

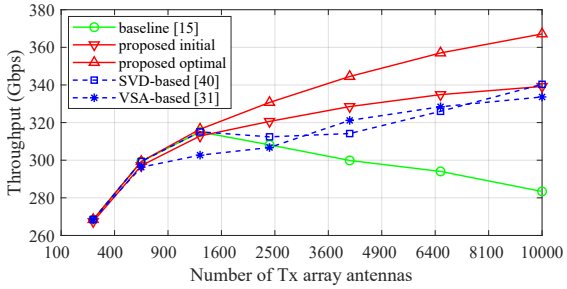

(a) Far-field scenario with $\varphi_{\mathrm{FP}}(x)$ and $\hat{\varphi}_{\mathrm{P}}(x)$

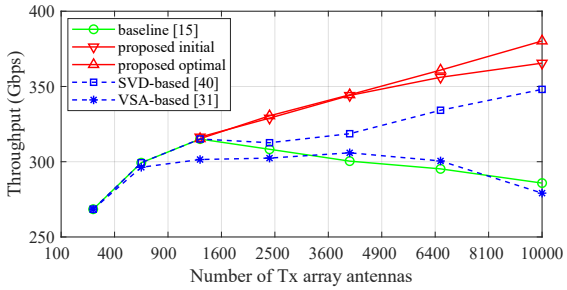

(b) Near-field scenario with $\varphi_{\mathrm{NP}}(x)$ and $\hat{\varphi}_{\mathrm{P}}(x)$

Fig. 17. TP versus Tx antenna number N_{T} in the UPA scenarios.

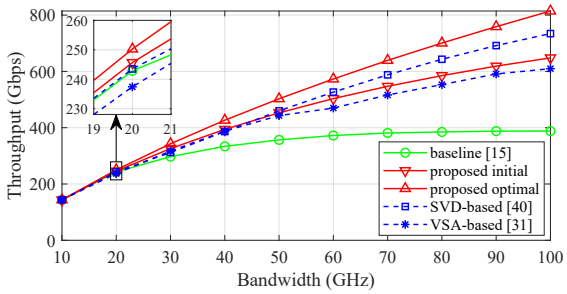

(a) Far-field scenario with $\varphi_{\mathrm{FP}}(x)$ and $\hat{\varphi}_{\mathrm{P}}(x)$

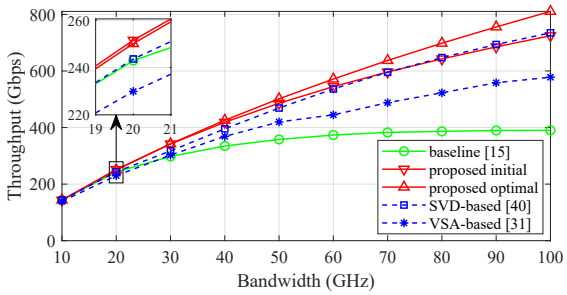

(b) Near-field scenario with $\varphi_{\mathrm{NP}}(x)$ and $\hat{\varphi}_{\mathrm{P}}(x)$

Fig. 18. TP versus bandwidth in the UPA scenarios.

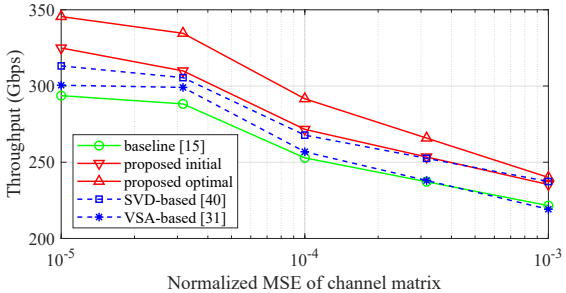

(a) Far-field scenario with $\varphi_{\mathrm{FP}}(x)$ and $\hat{\varphi}_{\mathrm{P}}(x)$

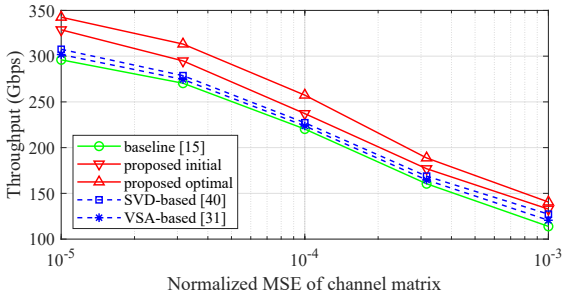

(b) Near-field scenario with $\varphi_{\mathrm{NP}}(x)$ and $\hat{\varphi}_{\mathrm{P}}(x)$

Fig. 19. TP versus MSE of channel $\vec{H}(f_m)$ in the UPA scenarios.

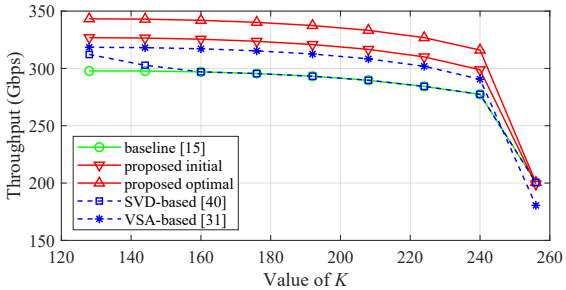

(a) Far-field scenario with $\varphi_{\mathrm{FP}}(x)$ and $\hat{\varphi}_{\mathrm{P}}(x)$

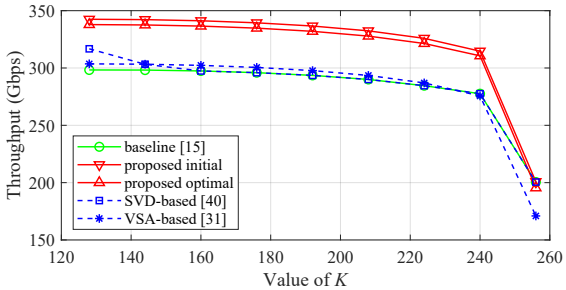

(b) Near-field scenario with $\varphi_{\mathrm{NP}}(x)$ and $\hat{\varphi}_{\mathrm{P}}(x)$

Fig. 20. TP versus number of middle band subcarriers K for non-uniform subcarrier allocation in the UPA scenarios.

Despite the reduction effect, the proposed solutions maintain the highest throughput, validating their effectiveness in such non-uniform allocation circumstances.

B. Results for the UPA Scenarios

To demonstrate the effect of the proposed solutions on the received signal power spectrum, Fig. 13 shows the value of $|g_{\mathrm{P}}(f)|^2$ in the UPA scenarios. Compared to the baselines and the initial phase functions, the optimal ones show much flatter curves of $|g_{\mathrm{P}}(f)|^2$, confirming their better anti-fading effect on signal power near the band edges.

Fig. 14 plots the throughput with respect to transmission power ρ_{t} for the proposed and other beamforming methods. The proposed optimal phase functions achieve the highest throughput, and the improvement is more significant than that in the ULA scenarios. Fig. 15 plots the BER versus ρ_{t}, in which the optimal phase functions achieve the best performance. Moreover, to demonstrate the applicability of the proposed solutions in practical phased array systems, Fig. 16 presents the throughput with respect to phase resolution, and shows that the optimal phase functions consistently achieve the best performance. These results demonstrate the superiority of our optimization method over other beamforming methods across these performance metrics.

Moreover, to explore the robustness of the proposed method, we evaluate the throughput versus N_{T}, BW, and channel estimation MSE as in the ULA scenarios. The results are presented by Fig. 17, Fig. 18, and Fig. 19, respectively. In all

the results, the proposed optimal phase functions consistently possess the highest throughput across different values of N_{T}, BW, and the MSE, validating the robustness of the proposed method under different conditions with the UPA configuration. Besides, throughput in the non-uniform subcarrier allocation case is also simulated, where the allocation pattern is the same as described in Section V-A. The result is shown in Fig. 20, where the proposed solutions maintain the highest throughput at different values of K, demonstrating a high adaptability of our method in such non-uniform allocation situations.

VI. Conclusion

We propose a spatial chirp-based optimization method for analog beamforming in LoS THz UWB systems, mitigating beam splitting and improving throughput. We evaluate both ULA and UPA in far-field and near-field scenarios. Simulations show our method achieves highest throughput and lowest BER versus state-of-the-art approaches, and is robust in certain situations. We characterize phase functions by few polynomial coefficients, and optimize them rather than entire massive phase shifters. Therefore, our approach is more efficient for complex scenarios like RIS-assisted massive arrays—a focus of ongoing research.

Appendix A
Derivation of $\varphi_{\mathrm{NL}}(x)$

Substituting $\mu_{\mathrm{NL}}(x)$ in Equation (9) into $\tilde{g}_{\mathrm{L}}(f)$ in Equation (15) and ignoring amplitude $\frac{1}{f\mu(x)}$ yields

$$|\tilde{g}_{\mathrm{L}}(f)| \propto \left| \int_{-\frac{L}{2}}^{\frac{L}{2}} e^{j\varphi_{\mathrm{NL}}(x)} e^{-j\frac{2\pi f \mu_{\mathrm{NL}}(x)}{c}} \mathrm{d}x \right|. \tag{45}$$

Let $s(x) = \mu_{\mathrm{NL}}(x)$, $s \in [s_1, s_2]$, $s_1 = \min\{\mu_{\mathrm{NL}}(x)\}$, $s_2 = \max\{\mu_{\mathrm{NL}}(x)\}$, giving $x(s) = D\cos\alpha \pm \sqrt{s^2 - (D\sin(\alpha))^2}$ and $\mathrm{d}x = \pm\frac{s}{\sqrt{s^2-(D\sin(\alpha))^2}}\mathrm{d}s$, where $\bar{D} = D\sin\alpha$. Let $\omega(f) = \frac{2\pi f}{c}$, $\omega \in [\omega_1, \omega_2] = [\frac{2\pi}{c}(f_{\mathrm{c}} - \frac{BW}{2}), \frac{2\pi}{c}(f_{\mathrm{c}} + \frac{BW}{2})]$, $\psi_{\mathrm{NL}}(s) = \varphi_{\mathrm{NL}}(x(s))$, and $\varrho_{\mathrm{L}}(\omega) = \tilde{g}_{\mathrm{L}}(f(\omega))$, it has

$$|\varrho_{\mathrm{L}}(\omega)| \propto \left| \int_{s_1}^{s_2} \frac{s}{\sqrt{s^2 - \bar{D}^2}} e^{j\psi_{\mathrm{NL}}(s)} e^{-j\omega s} \mathrm{d}s \right|. \tag{46}$$

Thus, $|\varrho_{\mathrm{L}}(\omega)| \propto |\mathcal{F}\{\eta_{\mathrm{NL}}(s)\}|$ where

$$\eta_{\mathrm{NL}}(s) = \begin{cases} \frac{s}{\sqrt{s^2-\bar{D}^2}} e^{j\psi_{\mathrm{NL}}(s)}, s \in [s_1, s_2] \\ 0, s \notin [s_1, s_2] \end{cases}. \tag{47}$$

By the SPM, uniform $|\varrho_{\mathrm{L}}(\omega)|^2$ in $[\omega_1, \omega_2]$ requires $\psi_{\mathrm{NL}}(s)$ to satisfy

$$\begin{cases} \psi''_{\mathrm{NL}}(s) \propto \frac{s^2}{s^2-\bar{D}^2} \\ \psi'_{\mathrm{NL}}(s_1) = \omega_1 \\ \psi'_{\mathrm{NL}}(s_2) = \omega_2 \end{cases}. \tag{48}$$

Setting $\psi''_{\mathrm{NL}}(s) = \frac{C_0 s^2}{s^2-\bar{D}^2}$ gives

$$\psi'_{\mathrm{NL}}(s) = \frac{C_0\bar{D}}{2}[\ln(|s-\bar{D}|) - \ln(s+\bar{D})] + C_0 s + C_1, \tag{49}$$

where C_0 and C_1 are constants. Since $\mu_{\mathrm{NL}}(x) \geq D\sin(\alpha), \forall\alpha \in [0,\pi]$ according to Equation (9), $|s-\bar{D}| = s - \bar{D}$. With $C_2 = \frac{\bar{D}}{2}[\ln(s_1-\bar{D}) - \ln(s_1+\bar{D})] + s_1$ and $C_3 = \frac{\bar{D}}{2}[\ln(s_2-\bar{D}) - \ln(s_2+\bar{D})] + s_2$, Equation (48) yields

$$\begin{cases} \psi'_{\mathrm{NL}}(s_1) = C_0C_2 + C_1 = \omega_1 \\ \psi'_{\mathrm{NL}}(s_2) = C_0C_3 + C_1 = \omega_2 \end{cases}. \tag{50}$$

Thus, $C_0 = \frac{\omega_2-\omega_1}{C_3-C_2}$, $C_1 = \frac{\omega_1 C_3 - \omega_2 C_2}{C_3-C_2}$, and

$$\begin{aligned} \psi_{\mathrm{NL}}(s) = \frac{C_0\bar{D}}{2}[(s-\bar{D})\ln(s-\bar{D}) \\ - (s+\bar{D})\ln(s+\bar{D})] + \frac{C_0}{2}s^2 + C_1 s + C_0\bar{D}^2 + C_4 \end{aligned} \tag{51}$$

where constant $C_0\bar{D}^2 + C_4$ is eliminated in $|\varrho_{\mathrm{L}}(\omega)|$. Finally, $\varphi_{\mathrm{NL}}(x)$ follows by substituting $s(x) = \mu_{\mathrm{NL}}(x)$ into $\psi_{\mathrm{NL}}(s)$.

Appendix B
Derivation of $\varphi_{\mathrm{NP}}(x, y)$

Substituting $\tilde{\mu}_{\mathrm{NP}}(x, y)$ in Equation (32) into $\tilde{g}_{\mathrm{P}}(f)$ in Equation (23) and ignoring amplitude $\frac{1}{f\mu(x)}$ yields

$$\begin{aligned} \tilde{g}_{\mathrm{P}}(f) \propto \int_{-\frac{L}{2}}^{\frac{L}{2}} \int_{-\frac{L}{2}}^{\frac{L}{2}} e^{j\varphi_{\mathrm{NP}}(x,y)} \times \\ e^{j\frac{2\pi f}{c}(k_0 + k_1 x + k_2 x^2 + k_3 y + k_4 y^2)} \mathrm{d}x\mathrm{d}y. \end{aligned} \tag{52}$$

By assuming

$$\varphi_{\mathrm{NP}}(x, y) = \tilde{\varphi}_{\mathrm{x}}(x) + \tilde{\varphi}_{\mathrm{y}}(y), \tag{53}$$

it has $\tilde{g}_{\mathrm{P}}(f) \propto \tilde{g}_{\mathrm{x}}(f)\tilde{g}_{\mathrm{y}}(f) e^{j\frac{2\pi f}{c}k_0}$, where

$$\tilde{g}_{\mathrm{x}}(f) = \int_{-\frac{L}{2}}^{\frac{L}{2}} e^{j\tilde{\varphi}_{\mathrm{x}}(x)} e^{j\frac{2\pi f}{c}(k_1 x + k_2 x^2)} \mathrm{d}x, \tag{54}$$

$$\tilde{g}_{\mathrm{y}}(f) = \int_{-\frac{L}{2}}^{\frac{L}{2}} e^{j\tilde{\varphi}_{\mathrm{y}}(y)} e^{j\frac{2\pi f}{c}(k_3 y + k_4 y^2)} \mathrm{d}y. \tag{55}$$

Uniform $|\tilde{g}_{\mathrm{P}}(f)|^2$ requires uniform $|\tilde{g}_{\mathrm{x}}(f)|^2$ and $|\tilde{g}_{\mathrm{y}}(f)|^2$, achievable via designing $\tilde{\varphi}_{\mathrm{x}}(x)$ and $\tilde{\varphi}_{\mathrm{y}}(y)$ using the SPM.

For $\tilde{\varphi}_{\mathrm{x}}(x)$, let $s(x) = -k_1 x - k_2 x^2$, $s \in [s_1, s_2] = [\min\{-k_1 x - k_2 x^2\}, \max\{-k_1 x - k_2 x^2\}]$, giving $x(s) = \frac{-k_1 \pm \sqrt{k_1^2 - 4k_2 s}}{2k_2}$ and $\mathrm{d}x = \mp\frac{1}{\sqrt{k_1^2-4k_2 s}}\mathrm{d}s$. With $\omega(f) = \frac{2\pi f}{c}$, $\psi_{\mathrm{x}}(s) = \tilde{\varphi}_{\mathrm{x}}(x(s))$, and $\varrho_{\mathrm{x}}(\omega) = \tilde{g}_{\mathrm{x}}(f(\omega))$, Equation (54) has

$$|\varrho_{\mathrm{x}}(\omega)| \propto \left| \int_{s_1}^{s_2} \frac{1}{\sqrt{k_1^2 - 4k_2 s}} e^{j\psi_{\mathrm{x}}(s)} e^{-j\omega s} \mathrm{d}s \right|. \tag{56}$$

Thus, $|\varrho_{\mathrm{x}}(\omega)| \propto |\mathcal{F}\{\eta_{\mathrm{x}}(s)\}|$ where

$$\eta_{\mathrm{x}}(s) = \begin{cases} \frac{1}{\sqrt{k_1^2-4k_2 s}} e^{j\psi_{\mathrm{x}}(s)}, s \in [s_1, s_2] \\ 0, s \notin [s_1, s_2] \end{cases}. \tag{57}$$

By SPM, uniform $|\varrho_{\mathrm{L}}(\omega)|^2$ in $[\omega_1, \omega_2]$ requires

$$\begin{cases} \psi''_{\mathrm{x}}(s) \propto \frac{1}{k_1^2-4k_2 s} \\ \psi'_{\mathrm{x}}(s_1) = \omega_1 \\ \psi'_{\mathrm{x}}(s_2) = \omega_2 \end{cases}. \tag{58}$$

Setting $\psi''_{\mathrm{NL}}(s) = \frac{C_0}{k_1^2-4k_2 s}$ gives

$$\psi'_{\mathrm{x}}(s) = -\frac{C_0}{4k_2}\ln(k_1^2 - 4k_2 s) + C_1, \tag{59}$$

where C_0 and C_1 are constants. With $C_2 = -\frac{\ln(k_1^2-4k_2s_1)}{4k_2}$ and $C_3 = -\frac{\ln(k_1^2-4k_2s_2)}{4k_2}$, Equation (58) yields

$$\begin{cases} \psi'_{\mathrm{x}}(s_1) = C_0C_2 + C_1 = \omega_1 \\ \psi'_{\mathrm{x}}(s_2) = C_0C_3 + C_1 = \omega_2 \end{cases}. \tag{60}$$

Thus, $C_0 = \frac{\omega_2-\omega_1}{C_3-C_2}$, $C_1 = \frac{\omega_1C_3-\omega_2C_2}{C_3-C_2}$, and

$$\psi_{\mathrm{x}}(s) = \frac{C_0}{16k_2^2}(k_1^2-4k_2s)(\ln(k_1^2-4k_2s)-1)+C_1s+C_4 \tag{61}$$

where C_4 is eliminated in $|\varrho_{\mathrm{x}}(\omega)|$. Similarly, $\psi_{\mathrm{y}}(s)$ follows using k_3 and k_4. Substituting $s(x)$ and $s(y)$ yields $\tilde{\varphi}_{\mathrm{x}}(x)$ and $\tilde{\varphi}_{\mathrm{y}}(y)$, giving $\varphi_{\mathrm{NP}}(x, y)$ via Equation (53).

ACKNOWLEDGMENT

This research was conducted as a collaborative team project. All authors made substantial and equal contributions to the conceptualization, methodology, analysis, and writing of this manuscript.

The work of Pingzhi Fan was supported by the National Natural Science Foundation of China (NSFC) under Project No.U23A20274 and No.62020106001.

REFERENCES

[1] A. Shafie, N. Yang, C. Han, J. M. Jornet, M. Juntti, and T. Kürner, "Terahertz communications for 6g and beyond wireless networks: Challenges, key advancements, and opportunities," *IEEE Network*, vol. 37, no. 3, pp. 162–169, May 2023.

[2] G. Singh, I. Verma, S. Bhardwaj, R. Sharma, and W. Ahmed, "Requirements, technologies, applications and challenges of 6g communication: A review," in *2024 IEEE International Conference on Computing, Power and Communication Technologies (IC2PCT)*, vol. 5, 2024, pp. 1608–1612.

[3] T. S. Rappaport, Y. Xing, O. Kanhere, S. Ju, A. Madanayake, S. Mandal, A. Alkhateeb, and G. C. Trichopoulos, "Wireless communications and applications above 100 ghz: Opportunities and challenges for 6g and beyond," *IEEE Access*, vol. 7, pp. 78 729–78 757, 2019.

[4] P. Bhattacharya, D. Saraswat, A. Dave, M. Acharya, S. Tanwar, G. Sharma, and I. E. Davidson, "Coalition of 6g and blockchain in ar/vr space: Challenges and future directions," *IEEE Access*, vol. 9, pp. 168 455–168 484, 2021.

[5] A. Paidimarri and B. Sadhu, "Spatio-temporal filtering: Precise beam control using fast beam switching," in *2020 IEEE Radio Frequency Integrated Circuits Symposium (RFIC)*, 2020, pp. 207–210.

[6] Y. Monnai, X. Lu, and K. Sengupta, "Terahertz beam steering: from fundamentals to applications," *Journal of infrared, millimeter and terahertz waves*, vol. 44, no. 3-4, pp. 169–211, Apr. 2023.

[7] B. Aqlan, M. Himdi, H. Vettikalladi, and L. Le-Coq, "Experimental realization of sub-thz circularly polarized antenna based on metasurface superstrate at 300 ghz," *Materials*, vol. 14, no. 17, p. 4796, Aug. 2021.

[8] A. S. Mohammed, G. Lévêque, E. Lebouvier, Y. Pennec, M. Faucher, A. Amo, P. Szriftgiser, and G. Ducournau, "Engineering the breaking of topological protection in valley photonic crystals enables to design chip level functions for thz 6g communications and beyond," *Journal of Lightwave Technology*, pp. 1–13, 2024.

[9] F. Sheikh, M. Alissa, A. Zahid, Q. H. Abbasi, and T. Kaiser, "Atmospheric attenuation analysis in indoor thz communication channels," in *2019 IEEE International Symposium on Antennas and Propagation and USNC-URSI Radio Science Meeting*, 2019, pp. 2137–2138.

[10] K. J. Jang, J. H. Oh, Y. Yoon, J. Kim, and G. Hwang, "Atmospheric attenuation model using gaussian process in sub-thz terrestrial wireless communications," *IEEE Antennas and Wireless Propagation Letters*, vol. 23, no. 2, pp. 568–572, Feb. 2024.

[11] Y. Mi and Q. Song, "Energy efficiency maximization for irs-aided wpcns," *IEEE Wireless Communications Letters*, vol. 10, no. 10, pp. 2304–2308, Oct. 2021.

[12] P. Skrimponis, N. Hosseinzadeh, A. Khalili, E. Erkip, M. J. W. Rodwell, J. F. Buckwalter, and S. Rangan, "Towards energy efficient mobile wireless receivers above 100 ghz," *IEEE Access*, vol. 9, pp. 20 704–20 716, 2021.

[13] R. Dilli, "Performance analysis of multi user massive mimo hybrid beamforming systems at millimeter wave frequency bands," *Wireless networks*, vol. 27, no. 3, pp. 1925–1939, Apr. 2021.

[14] T. Xu, C. Masouros, and I. Darwazeh, "Design and prototyping of hybrid analog–digital multiuser mimo beamforming for nonorthogonal signals," *IEEE Internet of Things Journal*, vol. 7, no. 3, pp. 1872–1883, Mar. 2020.

[15] B. Ning, W. Mei, L. Zhu, Z. Chen, and R. Zhang, "Max-min beamformer for thz wideband communications," in *2023 IEEE International Conference on Communications Workshops (ICC Workshops)*, 2023, pp. 1747–1752.

[16] M. Ma, N. Nguyen, and M. Juntti, "Switch-based hybrid beamforming for wideband multi-carrier communications," Nov. 2021.

[17] Y. Chen, D. Chen, and T. Jiang, "Beam-squint mitigating in reconfigurable intelligent surface aided wideband mmwave communications," in *2021 IEEE Wireless Communications and Networking Conference (WCNC)*, 2021, pp. 1–6.

[18] Y. Chen, Y. Xiong, D. Chen, T. Jiang, S. X. Ng, and L. Hanzo, "Hybrid precoding for wideband millimeter wave mimo systems in the face of beam squint," *IEEE Transactions on Wireless Communications*, vol. 20, no. 3, pp. 1847–1860, Mar. 2021.

[19] S.-H. Park, B. Kim, D. K. Kim, L. Dai, K.-K. Wong, and C.-B. Chae, "Beam squint in ultra-wideband mmwave systems: Rf lens array vs. phase-shifter-based array," *IEEE Wireless Communications*, vol. 30, no. 4, pp. 82–89, Aug. 2023.

[20] A. Liao, Z. Gao, D. Wang, H. Wang, H. Yin, D. W. K. Ng, and M.-S. Alouini, "Terahertz ultra-massive mimo-based aeronautical communications in space-air-ground integrated networks," *IEEE Journal on Selected Areas in Communications*, vol. 39, no. 6, pp. 1741–1767, Jun. 2021.

[21] W. Hao, F. Zhou, M. Zeng, O. A. Dobre, and N. Al-Dhahir, "Ultra wideband thz irs communications: Applications, challenges, key techniques, and research opportunities," *IEEE Network*, vol. 36, no. 6, pp. 214–220, Nov. 2022.

[22] X. Chen, P. Raj Gautam, and L. Zhang, "Low-complexity phase shifter design for reconfigurable intelligent surface aided mmwave massive mimo systems," in *2024 IEEE Wireless Communications and Networking Conference (WCNC)*, 2024, pp. 1–6.

[23] T. S. Priya, K. Manish, and P. Prakasam, "Hybrid beamforming for massive mimo using rectangular antenna array model in 5g wireless networks," *Wireless personal communications*, vol. 120, no. 3, pp. 2061–2083, Oct. 2021.

[24] S. Hamid, S. R. Chopra, A. Gupta, S. Tanwar, B. C. Florea, D. D. Taralunga, O. Alfarraj, and A. M. Shehata, "Hybrid beamforming in massive mimo for next-generation communication technology," *Sensors*, vol. 23, no. 16, p. 7294, Aug. 2023.

[25] N. T. Nguyen and K. Lee, "Unequally sub-connected architecture for hybrid beamforming in massive mimo systems," *IEEE Transactions on Wireless Communications*, vol. 19, no. 2, pp. 1127–1140, Feb. 2020.

[26] M. Majidzadeh, J. Kaleva, N. Tervo, H. Pennanen, A. Tolli, and M. Latva-aho, "Hybrid beamforming for mm-wave massive mimo systems with partially connected rf architecture," *Wireless personal communications*, vol. 136, no. 4, pp. 1947–1979, Jun. 2024.

[27] R. Rotman, M. Tur, and L. Yaron, "True time delay in phased arrays," *Proceedings of the IEEE*, vol. 104, no. 3, pp. 504–518, Mar. 2016.

[28] X. Liu and D. Qiao, "Space-time block coding-based beamforming for beam squint compensation," *IEEE Wireless Communications Letters*, vol. 8, no. 1, pp. 241–244, Feb. 2019.

[29] J. Tan and L. Dai, "Delay-phase precoding for thz massive mimo with beam split," in *2019 IEEE Global Communications Conference (GLOBECOM)*, 2019, pp. 1–6.

[30] B. Zhai, Y. Zhu, A. Tang, and X. Wang, "Thzprism: Frequency-based beam spreading for terahertz communication systems," *IEEE Wireless Communications Letters*, vol. 9, no. 6, pp. 897–900, Jun. 2020.

[31] F. Gao, B. Wang, C. Xing, J. An, and G. Y. Li, "Wideband beamforming for hybrid massive mimo terahertz communications," *IEEE Journal on Selected Areas in Communications*, vol. 39, no. 6, pp. 1725–1740, Jun. 2021.

[32] A. Elbir, K. Mishra, A. Celik, and A. Eltawil, "The curse of beam-squint in isac: Causes, implications, and mitigation strategies," *IEEE communications magazine*, vol. 62, no. 9, pp. 52–58, Jun. 2024.

[33] S. Xie, L. Li, Z. Chen, B. Ning, W. Chen, and S. Li, "Improving thz transmission distance for delay-sensitive services via mobile computing,"

IEEE Transactions on Vehicular Technology, vol. 72, no. 2, pp. 2051–2065, Feb. 2023.
[34] Y. Xie, B. Ning, L. Li, and Z. Chen, "Near-field beam training in thz communications: The merits of uniform circular array," *IEEE Wireless Communications Letters*, vol. 12, no. 4, pp. 575–579, Apr. 2023.
[35] M. Cui, Z. Wu, Y. Lu, X. Wei, and L. Dai, "Near-field mimo communications for 6g: Fundamentals, challenges, potentials, and future directions," *IEEE Communications Magazine*, vol. 61, no. 1, pp. 40–46, Jan. 2023.
[36] K. H. Sayidmarie and Q. H. Sultan, "Synthesis of wide beam array patterns using quadratic-phase excitations," *Int. J. Electromagn. Appl*, vol. 3, no. 6, p. 127–135, 2013.
[37] V. Sergeev, A. Davydov, G. Morozov, O. Orhan, and W. Lee, "Enhanced precoding design with adaptive beam width for 5g new radio systems," in *2017 IEEE 86th Vehicular Technology Conference (VTC-Fall)*, 2017, pp. 1–5.
[38] N. J. Myers and R. W. Heath, "Infocus: A spatial coding technique to mitigate misfocus in near-field los beamforming," *IEEE Transactions on Wireless Communications*, vol. 21, no. 4, pp. 2193–2209, Apr. 2022.
[39] Z. Huang, R. Prüller, S. Schwarz, and M. Rupp, "Misfocus-reduction in ris-assisted ultra-wideband wireless communication," in *2023 Joint European Conference on Networks and Communications 6G Summit (EuCNC/6G Summit)*, 2023, pp. 108–113.
[40] C. Fonteneau, M. Crussière, and B. Jahan, "An efficient analog eigen-beamforming procedure for wideband mmwave mimo-ofdm systems," in *2022 IEEE 23rd International Symposium on a World of Wireless, Mobile and Multimedia Networks (WoWMoM)*, 2022, pp. 214–220.
[41] C. A. Balanis, *Antenna theory: analysis and design*, 4th ed. Hoboken, New Jersey: Wiley, 2016.
[42] K. T. Selvan and R. Janaswamy, "Fraunhofer and fresnel distances: Unified derivation for aperture antennas," *IEEE Antennas and Propagation Magazine*, vol. 59, no. 4, pp. 12–15, Aug. 2017.
[43] H. Wymeersch, "A fisher information analysis of joint localization and synchronization in near field," in *2020 IEEE International Conference on Communications Workshops (ICC Workshops)*, 2020, pp. 1–6.
[44] Y. Han, S. Jin, C.-K. Wen, and X. Ma, "Channel estimation for extremely large-scale massive mimo systems," *IEEE Wireless Communications Letters*, vol. 9, no. 5, pp. 633–637, May 2020.
[45] Z.-Q. He and X. Yuan, "Cascaded channel estimation for large intelligent metasurface assisted massive mimo," *IEEE Wireless Communications Letters*, vol. 9, no. 2, pp. 210–214, Feb. 2020.
[46] J. Wang, C.-X. Wang, J. Huang, H. Wang, X. Gao, X. You, and Y. Hao, "A novel 3d non-stationary gbsm for 6g thz ultra-massive mimo wireless systems," *IEEE Transactions on Vehicular Technology*, vol. 70, no. 12, pp. 12 312–12 324, Dec. 2021.
[47] M. Cui and L. Dai, "Channel estimation for extremely large-scale mimo: Far-field or near-field?" *IEEE Transactions on Communications*, vol. 70, no. 4, pp. 2663–2677, Apr. 2022.
[48] V. A. Borovikov, *Uniform stationary phase method*. London : Institution of Electrical Engineers, 1994.
[49] J. R. Klauder, A. C. Price, S. Darlington, and W. J. Albersheim, "The theory and design of chirp radars," *The Bell System Technical Journal*, vol. 39, no. 4, pp. 745–808, Jul. 1960.
[50] A. Moldovan, M. A. Ruder, I. F. Akyildiz, and W. H. Gerstacker, "Los and nlos channel modeling for terahertz wireless communication with scattered rays," in *2014 IEEE Globecom Workshops (GC Wkshps)*, 2014, pp. 388–392.

Xingyu Chen received the B.Eng. degree in Electronic and Electrical Engineering from the University of Leeds, Leeds, U.K., and Southwest Jiaotong University (SWJTU), Chengdu, China, in 2022. He is currently pursuing the Ph.D. degree with the School of Electronic and Electrical Engineering, University of Leeds, where his research focuses on reconfigurable intelligent surface (RIS) enabled massive MIMO communication systems. His research interests include RIS, MIMO systems, beamforming, millimeter-wave and terahertz communications, ultra-wideband OFDM systems, and large-scale phased array systems.

Li Zhang is an Associate Professor in Communications at the School of Electronic and Electrical Engineering, University of Leeds, where she leads the Wireless Communication Group. Her research focuses on massive MIMO, mmWave and THz communications, Non-Terrestrial Networks (NTNs), mobile edge computing and 5G/6G systems. She has served on the Technical Programme Committees of most major IEEE communications conferences and is currently an associate editor for several IEEE journals. She has been a member of the UK EPSRC Peer Review College since 2006 and has served on grant review panels for both EPSRC and Royal Society. She also regularly reviews grant proposals for international funding bodies, including the Qatar National Research Fund, and agencies in Denmark and France, as well as book proposals for various academic publishers. She has acted as a PhD examiner for numerous universities within and outside the UK. She received a Nuffield Award for newly appointed lecturers in 2005, became a Fellow of the Higher Education Academy in 2006, and was elevated to IEEE Senior Member in 2012.

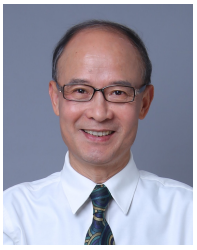

Pingzhi Fan (Fellow, IEEE) received the M.Sc. degree in computer science from Southwest Jiaotong University, China, in 1987, and the Ph.D. degree in electronic engineering from Hull University, U.K., in 1994. He is currently a distinguished professor of Southwest Jiaotong University (SWJTU), honorary dean of the SWJTU-Leeds Joint School (2015-), honorary professor of the University of Nottingham (Ningbo, 2025), and a visiting professor of Leeds University, UK (1997-). He is a recipient of the UK ORS Award (1992), the National Science Fund for Distinguished Young Scholars (1998, NSFC), IEEE VT Society Jack Neubauer Memorial Award (2018), IEEE SP Society SPL Best Paper Award (2018), IEEE VT Society Best Magazine Paper Award (2023), and several IEEE conference best paper awards. He served as chief scientist of a National 973 Plan Project (MoST, 2012.1-2016.12). He also served as general chair or TPC chair of a number of IEEE conferences, including VTC2016Spring, ITW2018, IWSDA2022, PIMRC2023, VTC2025Fall, as well as the coming ISIT2026, ICC2028. His research interests include high mobility wireless communications, multiple access techniques, ISAC, signal design & coding, etc. He is an IEEE VTS Distinguished Speaker (2022-2028), a fellow of IEEE, IET, CIE and CIC.